

# Sub-structure and merger detection in resolved NIKA Sunyaev-Zel'dovich images of distant clusters

R. Adam<sup>1,2\*</sup>, O. Hahn<sup>1</sup>, F. Ruppin<sup>2</sup>, P. Ade<sup>5</sup>, P. André<sup>4</sup>, M. Arnaud<sup>4</sup>, I. Bartalucci<sup>4</sup>, A. Beelen<sup>6</sup>, A. Benoît<sup>7</sup>, A. Bideaud<sup>7</sup>, N. Billot<sup>8</sup>, O. Bourrion<sup>2</sup>, M. Calvo<sup>7</sup>, A. Catalano<sup>2</sup>, G. Coiffard<sup>3</sup>, B. Comis<sup>2</sup>, A. D'Addabbo<sup>7,9</sup>, F.-X. Désert<sup>10</sup>, S. Doyle<sup>5</sup>, C. Ferrari<sup>1</sup>, J. Goupy<sup>7</sup>, C. Kramer<sup>8</sup>, G. Lagache<sup>11</sup>, S. Leclercq<sup>3</sup>, J.-F. Lestrade<sup>17</sup>, J.F. Macías-Pérez<sup>2</sup>, G. Martínez Aviles<sup>1</sup>, D. Martizzi<sup>18</sup>, S. Maurogordato<sup>1</sup>, P. Mauskopf<sup>5,12</sup>, F. Mayet<sup>2</sup>, A. Monfardini<sup>7</sup>, F. Pajot<sup>6</sup>, E. Pascale<sup>5</sup>, L. Perotto<sup>2</sup>, G. Pisano<sup>5</sup>, E. Pointecouteau<sup>19,20</sup>, N. Ponthieu<sup>10</sup>, G.W. Pratt<sup>4</sup>, V. Revéret<sup>4</sup>, M. Ricci<sup>1</sup>, A. Ritacco<sup>8</sup>, L. Rodriguez<sup>4</sup>, C. Romero<sup>3</sup>, H. Roussel<sup>16</sup>, K. Schuster<sup>3</sup>, A. Sievers<sup>8</sup>, S. Triqueneaux<sup>7</sup>, C. Tucker<sup>5</sup>, H.-Y. Wu<sup>21</sup>, and R. Zylka<sup>3</sup>

<sup>1</sup> Laboratoire Lagrange, Université Côte d'Azur, Observatoire de la Côte d'Azur, CNRS, Blvd de l'Observatoire, CS 34229, 06304 Nice cedex 4, France

<sup>2</sup> Laboratoire de Physique Subatomique et de Cosmologie, Université Grenoble Alpes, CNRS/IN2P3, 53, avenue des Martyrs, Grenoble, France

<sup>3</sup> Institut de RadioAstronomie Millimétrique (IRAM), Grenoble, France

<sup>4</sup> Laboratoire AIM, CEA/IRFU, CNRS/INSU, Université Paris Diderot, CEA-Saclay, 91191 Gif-Sur-Yvette, France

<sup>5</sup> Astronomy Instrumentation Group, University of Cardiff, UK

<sup>6</sup> Institut d'Astrophysique Spatiale (IAS), CNRS and Université Paris Sud, Orsay, France

<sup>7</sup> Institut Néel, CNRS and Université Grenoble Alpes, France

<sup>8</sup> Institut de RadioAstronomie Millimétrique (IRAM), Granada, Spain

<sup>9</sup> Dipartimento di Fisica, Sapienza Università di Roma, Piazzale Aldo Moro 5, I-00185 Roma, Italy

<sup>10</sup> Univ. Grenoble Alpes, CNRS, IPAG, F-38000 Grenoble, France

<sup>11</sup> Aix Marseille Université, CNRS, LAM (Laboratoire d'Astrophysique de Marseille) UMR 7326, 13388, Marseille, France

<sup>12</sup> School of Earth and Space Exploration and Department of Physics, Arizona State University, Tempe, AZ 85287

<sup>13</sup> Université de Toulouse, UPS-OMP, Institut de Recherche en Astrophysique et Planétologie (IRAP), Toulouse, France

<sup>14</sup> CNRS, IRAP, 9 Av. colonel Roche, BP 44346, F-31028 Toulouse cedex 4, France

<sup>15</sup> University College London, Department of Physics and Astronomy, Gower Street, London WC1E 6BT, UK

<sup>16</sup> Institut d'Astrophysique de Paris, Sorbonne Universités, UPMC Univ. Paris 06, CNRS UMR 7095, 75014 Paris, France

<sup>17</sup> LERMA, CNRS, Observatoire de Paris, 61 avenue de l'Observatoire, Paris, France

<sup>18</sup> Department of Astronomy, University of California, Berkeley, CA 94720-3411, USA

<sup>19</sup> Université de Toulouse, UPS-OMP, Institut de Recherche en Astrophysique et Planétologie (IRAP), Toulouse, France

<sup>20</sup> CNRS, IRAP, 9 Av. colonel Roche, BP 44346, F-31028 Toulouse cedex 4, France

<sup>21</sup> California Institute of Technology, MC 367-17, Pasadena, CA 91125, USA.

Received September 14, 2017 / Accepted –

## Abstract

Sub-structures in the hot gas atmosphere of galaxy clusters are related to their formation history and to the astrophysical processes at play in the intracluster medium (ICM). The thermal Sunyaev-Zel'dovich (tSZ) effect is directly sensitive to the line-of-sight integrated ICM pressure, and is thus particularly adapted to study ICM sub-structures. In this paper, we apply structure-enhancement filtering algorithms to high resolution tSZ observations (e.g. NIKA) of distant clusters, in order to search for pressure discontinuities, compressions, as well as secondary peaks in the ICM. The same filters are applied to toy-model images and to synthetic tSZ images extracted from RHAPSODY-G cosmological hydrodynamic simulations, in order to better interpret the extracted features. We also study the noise propagation through the filters and quantify the impact of systematic effects, such as data processing induced artifacts and point source residuals, the latter being identified as the dominant potential contaminant. In three of our six NIKA-observed clusters we identify features at high signal-to-noise that show clear evidence for merger events. In MACS J0717.5+3745 ( $z = 0.55$ ), three strong pressure gradients are observed on the east, southeast and west sectors, and two main peaks in the pressure distribution are identified. We observe a lack of tSZ compact structure in the cool-core cluster PSZ1 G045.85+57.71 ( $z = 0.61$ ), and a tSZ gradient ridge dominates in the southeast. In the highest redshift cluster, CL J1226.9+3332 ( $z = 0.89$ ), we detect a  $\sim 45$  arcsec (360 kpc) long ridge pressure gradient associated with a secondary pressure peak in the west region. Our results show that current tSZ facilities have now reached the angular resolution and sensitivity to allow an exploration of the details of pressure sub-structures in clusters, even at high redshift. This opens the possibility to quantify the impact of the dynamical state on the relation between the tSZ signal and the mass of clusters, which is important when using tSZ clusters to test cosmological models. This work also marks the first NIKA cluster sample data release.

**Key words.** Techniques: high angular resolution; image processing – Galaxies: clusters: intracluster medium

## 1. Introduction

The internal structure of the hot ionized gas in galaxy clusters reflects their formation through the hierarchical merging of smaller structures and groups, and the accretion of surrounding material (e.g. Kravtsov & Borgani 2012, and references therein). It is tightly connected to turbulence, shocks and sloshing (e.g. Markevitch & Vikhlinin 2007) in the intracluster medium (ICM), as well as various non-gravitational physical processes such as feedback from compact sources (e.g. Fabian 2012). The study of the structure of the ICM is therefore a unique way to understand how clusters form, and to assess connections with the astrophysics at play. As the intracluster gas is commonly used to trace the overall mass distribution of clusters, an investigation of cluster astrophysics is in turn essential to handle scatter and biases that arise in the mass–observable relations, which are fundamental when using clusters as cosmological probes (see, e.g. Allen et al. 2011, for a review).

The thermal Sunyaev-Zel'dovich (tSZ, Sunyaev & Zel'dovich 1972) effect provides a direct probe of the integrated electron pressure along the line-of-sight in clusters. It is thus an excellent diagnostic of the thermodynamical properties of the ICM that are induced by gravitational dynamics and complements well X-ray imaging, which is sensitive to the squared electron density with weak temperature dependance. X-ray surface brightness provides a high density contrast, but cannot distinguish between cold front and shocks. The latter are accessible via the tSZ surface brightness through the pressure, but discontinuities that are in quasi-pressure equilibrium (e.g. cavities, cold fronts) will remain invisible in the tSZ signal, while they will show up in the X-ray. In addition, the tSZ effect is well suited to study distant clusters since, unlike other probes, its surface brightness is insensitive to distance.

The study of sub-structures in the ICM is now routinely applied to X-ray imaging. Dedicated filtering techniques have been developed in the literature, such as unsharp masking, or gradient filtering (see, for example, recent results by Sanders et al. 2016), highlighting ongoing physical processes in clusters, which would be missed otherwise (e.g. cold/shock front, jet cavity, sound waves, etc). However, only few applications of such procedures have been performed using tSZ data (see e.g. Bourdin et al. 2015, using simulated nearby Planck clusters). Indeed, these methods require both high angular resolution and high sensitivity observations, in order to obtain significant detections, and the corresponding data remain challenging to obtain beyond the local universe. With the advent of new state-of-the-art millimeter wave high angular resolution instruments such as NIKA2, installed on the IRAM 30m telescope (The New IRAM KIDs Array 2,  $< 20$  arcsec resolution at 150 and 260 GHz, Calvo et al. 2016; Catalano et al. 2016; Adam et al. 2017a), or MUSTANG2, on the Green Bank Telescope (The MUltiplexed Squid Tes Array at Ninety Gigahertz 2,  $\sim 8$  arcsec at 90 GHz, Dicker et al. 2014), the use of tSZ data to study the inner structure of clusters is about to enter a new era. Alternatively, the use of interferometers such as ALMA (Atacama Large Millimeter/submillimeter Array) have already shown the huge potential of such observations to map the tSZ effect at unprecedented angular resolutions (Kitayama et al. 2016; Basu et al. 2016).

The NIKA2 pathfinder, NIKA (Monfardini et al. 2011; Catalano et al. 2014), has already been used to image galaxy clusters at high angular resolution, including deep observations

(Adam et al. 2014, 2015, 2016, 2017c; Ruppin et al. 2017). In this paper, we apply filtering methods to the NIKA tSZ maps in order to detect and study pressure sub-structures in the ICM of six clusters of galaxies at  $0.45 \leq z \leq 0.89$ . The same filtering methods are applied to toy models and to synthetic tSZ maps extracted from the RHAPSODY-G hydrodynamical simulations (Wu et al. 2013; Hahn et al. 2017) to provide a better interpretation of the observed structures. We also study the noise propagation through the filters and quantify possible systematic effects arising from contaminating point sources and data processing. The detection of sub-structures allows us to infer the presence of ongoing merger activity of the targets and show the huge potential of future instrument for investigating cluster formation in distant clusters.

This paper is organized as follow. Section 2 describes the filtering algorithms. In Section 3 and 4, we apply the filtering procedure to toy models and to the RHAPSODY-G simulations. We investigate possible systematic effects and study the noise properties in Section 5. Finally, the filtering algorithms are applied to the NIKA cluster sample in Section 6 and we discuss their implications in Section 7. Summary and conclusions are provided in Section 8. Throughout this paper, we assume a flat  $\Lambda$ CDM cosmology according to *Planck* results (Planck Collaboration et al. 2016b) with  $H_0 = 67.8 \text{ km s}^{-1} \text{ Mpc}^{-1}$ ,  $\Omega_M = 0.308$ , and  $\Omega_\Lambda = 0.692$ .

## 2. Detection of pressure sub-structures

### 2.1. The thermal Sunyaev-Zel'dovich effect

The tSZ effect consists in the spectral distortion of the black-body spectrum of the cosmic microwave background (CMB) radiation. Its frequency dependence is given by (Birkinshaw 1999)

$$f(x, T_e) = \frac{x^4 e^x}{(e^x - 1)^2} \left( x \coth\left(\frac{x}{2}\right) - 4 \right) (1 + \delta_{\text{tSZ}}(x, T_e)), \quad (1)$$

where  $x = \frac{h\nu}{k_B T_{\text{CMB}}}$  is the dimensionless frequency,  $h$  the Planck constant,  $k_B$  the Boltzmann constant,  $\nu$  the observation frequency, and  $T_{\text{CMB}}$  the temperature of the CMB. The term  $\delta_{\text{tSZ}}(x, T_e)$  corresponds to relativistic corrections, which depend on the observing frequency and the electron temperature  $T_e$  (see, e.g. Itoh & Nozawa 2003). The induced change in intensity with respect to the primary CMB intensity,  $I_0$ , can be expressed as

$$\frac{\Delta I_{\text{tSZ}}}{I_0} = y f(x, T_e), \quad (2)$$

where  $y$  is the Compton parameter, which measures the integrated electronic pressure,  $P_e$ , along the line-of-sight,  $d\ell$ , written as

$$y = \frac{\sigma_T}{m_e c^2} \int P_e d\ell. \quad (3)$$

The parameter  $\sigma_T$  is the Thomson cross-section,  $m_e$  is the electron rest mass, and  $c$  the speed of light. In this paper, we are using the NIKA 150 GHz data only, frequency at which the tSZ signal is close to its maximum decrement. The NIKA maps thus provide a direct measurement of the line-of-sight integrated electron pressure assuming relativistic effects are small.

### 2.2. NIKA data

NIKA has been used to map six clusters of galaxies using the tSZ effect at 150 and 260 GHz between November 2012 and

\* Corresponding author: Rémi Adam, remi.adam@oca.eu

February 2015. This sample contains both well known objects with various multi-wavelength coverage and Planck discovered sources, at intermediate and high redshifts. The names, coordinates, and main properties of the clusters are listed in Table 1, and by design, the sample contains a wide variety of cluster morphologies, spanning redshifts between 0.45 and 0.89. It was dedicated to provide pilot observations to test the feasibility of the NIKA2 (Adam et al. 2017a) tSZ Large Program, which is under preparation (Comis et al. 2016; Mayet et al. 2017).

The main steps of the data reduction are described in Adam et al. (2014, 2015). The reduction of the raw NIKA data affects the reconstructed astrophysical sky signal by filtering out structures on large scales. We compute the angular transfer function of the reduction, as described in Adam et al. (2015) and use it to deconvolve the data to compensate for filtering effects. The absolute zero level of the brightness on the map remains unconstrained when observing clusters with NIKA, and it cannot be corrected using the transfer function of the processing. This corresponds to the transfer function being zero at angular wavenumber  $k = 0$ . In this paper, we use the NIKA 150 GHz tSZ maps only, deconvolved from the transfer function except for the beam smoothing (see Section 5.2). The overall calibration uncertainty is estimated to be about 10% depending on the observation campaign (see Table 1), including the brightness temperature model of our primary calibrator, the NIKA bandpass uncertainties, the opacity correction, and the stability of the instrument (Catalano et al. 2014). All clusters are contaminated by foreground and/or background galaxies that appear as point sources in the maps and they are removed according to the procedure described in Adam et al. (2015) and Adam et al. (2016).

The NIKA maps,  $M$ , are produced on  $2 \text{ arcsec} \times 2 \text{ arcsec}$  pixel grids to ensure proper Nyquist sampling, with respect to the 18.2 arcsec FWHM beam. On small scales, the data are dominated by Gaussian noise. The peak signal-to-noise, after smoothing the maps at a 22 arcsec FWHM resolution, depends strongly on the observing time and weather conditions, ranging from  $\sim 4\sigma$  to about  $20\sigma$  for the deepest observations. As an example, Figure 1 provides the raw image of one of the NIKA cluster, MACS J0717.5+3745, to illustrate the nature of the data.

### 2.3. Algorithms

In order to reveal pressure sub-structures, we make use of two algorithms, namely a Gaussian Gradient Magnitude (GGM, see also Sanders et al. 2016) filter and a Difference of Gaussians (DoG) filter. They allow us to identify strong pressure gradients or discontinuities, and pressure peaks at specific scales, respectively.

#### 2.3.1. Gaussian gradient magnitude filter

Because the NIKA data are dominated by noise on small scales, we convolve the maps with a Gaussian kernel,  $G_{\theta_0}$ , of FWHM  $\theta_0$ , to reduce it. We then compute the magnitude of the gradient of the maps as

$$M_{\text{GGM}} = \sqrt{(\mathcal{D}_{\text{R.A.}} * [G_{\theta_0} * M])^2 + (\mathcal{D}_{\text{Dec.}} * [G_{\theta_0} * M])^2}, \quad (4)$$

where the convolution kernel  $\mathcal{D}_{\text{R.A.,Dec.}}$  along the R.A. and Dec. axis, are respectively given by

$$\mathcal{D}_{\text{R.A.}} = \mathcal{D}_{\text{Dec.}}^T = \frac{1}{8\Delta\theta} \begin{pmatrix} -1 & 0 & 1 \\ -2 & 0 & 2 \\ -1 & 0 & 1 \end{pmatrix}, \quad (5)$$

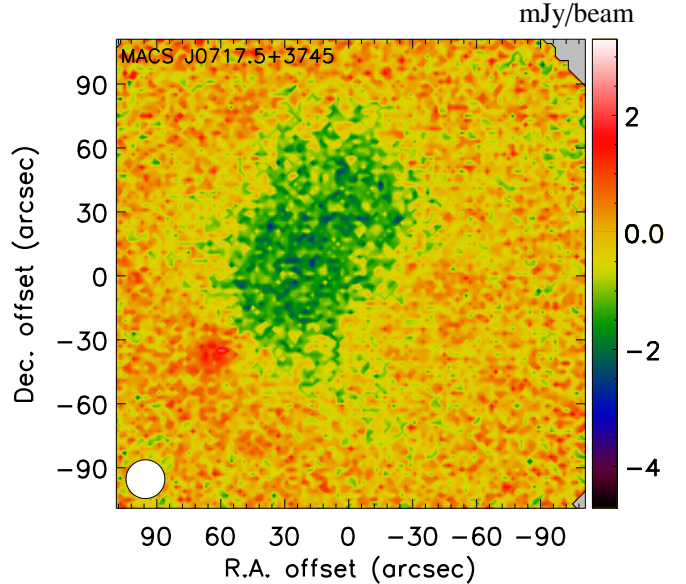


**Figure 1.** Example of the raw surface brightness image of MACS J0717.5+3745, prior to any filter application (e.g. smoothing), point source removal and deconvolution. The data is dominated by noise on small scales. The cluster diffuse emission is nonetheless visible as a negative decrement, as well as a radio foreground galaxy (positive) on the southeast. The white circle on the bottom left corner provide the NIKA beam FWHM.

where  $\Delta\theta$  is the map pixel size. The resulting quantity,  $M_{\text{GGM}}$ , is therefore a measurement of the projected pressure gradient on scale  $\theta_0$ . It is expressed in units of surface brightness per arcmin, and can be converted to physical units of keV/cm<sup>3</sup> Mpc per Mpc accounting for the angular diameter distance of the cluster and the conversion coefficients from Compton parameter to Jy/beam given in Adam et al. (2017c).

The direction of the gradient is obtained by computing its orientation on the sky, given by the angle

$$\Psi = \text{atan} \left( \frac{\mathcal{D}_{\text{Dec.}} * [G_{\theta_0} * M]}{\mathcal{D}_{\text{R.A.}} * [G_{\theta_0} * M]} \right). \quad (6)$$

#### 2.3.2. Difference of Gaussian filter

In order to extract pressure sub-structures on a specific scale, we compute the difference of the NIKA maps convolved respectively with Gaussian kernels of FWHM  $\theta_1$  and  $\theta_2$ :

$$M_{\text{DoG}} = G_{\theta_1} * M - G_{\theta_2} * M. \quad (7)$$

The filter thus removes signal on scales larger than  $\theta_2$  and on scale smaller than  $\theta_1$ , allowing us to search for structures in a narrow range of angular scales. The resulting map is homogeneous to the input map, i.e. it is sensitive to the projected pressure along the line-of-sight in the selected range of angular scales.

#### 2.3.3. Baseline filtering parameters

The NIKA beam FWHM is 18.2 arcsec at 150 GHz (Catalano et al. 2014). On small scales, the noise dominates over the signal and therefore, the smallest scale at which we can search for sub-structures is slightly below, but of the order of the beam FWHM, depending on the signal-to-noise of the data. As the data reduction attenuates the signal on scales larger than  $\sim 2$

**Table 1.** Summary of the main properties of the NIKA cluster sample, ordered by increasing redshift.

Name	$z$	kpc/arcsec	$M_{500}$ ( $10^{14} M_\odot$ )	$Y_{500}$ ( $10^{-3} \text{arcmin}^2$ )	Comments	Configuration	Calibration uncertainty	Projected time (hour)	Central rms <sup>(b)</sup> (mJy/beam)
RX J1347.5-1145	0.452	5.9	11.0	1.40	Cool-core+merger	Nov. 2012, preliminary instrument	15%	5.8	1.2
MACS J1423.8+2404	0.545	6.6	4.9 <sup>(a)</sup>	0.47 <sup>(a)</sup>	Relaxed elliptical cool-core	Feb. 2014, Open Pool	7%	1.5	0.35
MACS J0717.5+3745	0.546	6.6	11.5	1.74	Multiple merger, strong kSZ	Jan./Feb. 2014 & 2015, Open Pool	7%	13.1	0.10
PSZ1 G046.13+30.75	0.569	6.7	6.4	0.70	Disturbed	Nov. 2015, Open Pool	9%	6.0	0.32
PSZ1 G045.85+57.71	0.611	6.9	7.0	0.92	Elliptical cool-core	Nov. 2015, Open Pool	9%	6.4	0.17
CL J1226.9+3322	0.888	8.0	5.7	0.90	Disturbed core	Feb. 2014, Open Pool	7%	7.8	0.17

**Notes.** The masses are extracted from the *Planck* catalog (Planck Collaboration et al. 2016a). The integrated Compton parameter,  $Y_{500}$ , is computed by normalizing  $Y_{5R_{500}}$  (extracted from the *Planck* catalog) by a factor of 1.79, assuming a Universal pressure profile (Arnaud et al. 2010). <sup>(a)</sup> From Adam et al. (2016), as this cluster is not in the *Planck* catalog. <sup>(b)</sup> At the 22 arcsec FWHM effective angular resolution.

arcmin (see Adam et al. 2015, and Section 5), the signal is also dominated by noise on large scales. Consequently the spatial dynamics accessible with NIKA data is about one order of magnitude, between 15 and 150 arcsec. Here, we aim at detecting pressure discontinuities and compression regions in distant clusters ( $z > 0.4$ ), which requires to probe the smallest scales available. If present, sub-components are expected to have typical angular size smaller than that of the main clusters ( $\sim 1\text{--}2$  arcmin) by a factor of a few. Therefore, we focus on the following baseline parameters for our filters:  $\theta_0 = 15$  arcsec, and  $(\theta_1, \theta_2) = (15, 45)$  arcsec. In practice, it is possible to increase the signal-to-noise ratio of the filtered maps by increasing the filters scales, at the cost of washing out the signal arising from the sub-structures we aim to detect. In Appendix A, we show how the extracted signal changes according to the filter parameters.

### 3. Application to cluster toy models

The filtering algorithms are first tested on toy models in order to highlight the signature of the filtered signal in idealized physical situations. The toy models that we consider are: a spherical generalized Navarro Frenk and White (gNFW) pressure profile (Nagai et al. 2007), a bimodal pre-merging system, a main core plus an extension, and a pressure profile that includes a shock, respectively. We apply the filters using the baseline parameters discussed in Section 2.3.3.

#### 3.1. Construction of toy models

The construction of the toy models is described below. The clusters redshift are  $z = 0.6$  because it corresponds to the mean redshift of the NIKA sample (see Section 2.2 and Table 1), but we also test other redshifts between  $z = 0.4$  and  $z = 1$ .

**1. Spherical gNFW profile:** one of the most common and simple description of clusters pressure is that of a spherically symmetric radial distribution following a gNFW (Nagai et al. 2007) profile, and before using the filtered maps to investigate disturbances in the ICM, it is important to understand the response of the filters to perfectly spherical cluster signals. We thus simulate such a cluster using the best fit slopes and concentration parameters obtained by Planck Collaboration et al. (2013) and assuming a characteristic radius  $R_{500} = 1000$  kpc (comparable to NIKA clusters). The pressure is integrated along the line of sight, to produce an azimuthally symmetric Compton parameter map (Eq. 3), which we convert into surface brightness in the 150 GHz NIKA band (Eq. 1). We also use best fit parameter profiles of cool-core and disturbed clusters from Arnaud et al. (2010) to test changes in the steepness of the profile.

**2. Bimodal pre-merger system:** clusters can form via the merging of sub-clusters and groups. We model such system

using our gNFW model to simulate a pair of identical clusters, separated by 100 arcsec. We add a pressure bar component between the two clusters to mimic the adiabatic compression caused by the merger. The bar has an arbitrary projected size of  $R_{500}/5$  along the merger direction and  $R_{500}/1.5$  in the perpendicular direction. The tSZ amplitude of the bar is 0.3 times that of the gNFW components peaks.

- Main core plus extension:** it is common to find clusters made of a main core plus an extension that arises from both post-merger and pre-merger disturbances in the ICM. We model this system by a main gNFW cluster, to which we add a second gNFW sub-cluster with  $R_{500} = 300$  kpc, normalized to a peak of 1/3 that of the main core, and located 50 arcsec away.
- Shocks:** merging events can cause discontinuities in the ICM gas, such as shocks in the pressure. We thus simulate a radially symmetric cluster including a pressure discontinuity in the profile. We use the Rankine-Hugoniot jump conditions (see e.g. Sarazin 2002, for a review), given by  $\frac{P_1}{P_2} = \frac{2\gamma_{\text{ad}}}{\gamma_{\text{ad}} + 1} \mathcal{M}^2 + \frac{\gamma_{\text{ad}} - 1}{\gamma_{\text{ad}} + 1}$ , with  $P_1$  and  $P_2$  the pressure before and after the shock and  $\gamma_{\text{ad}} = 5/3$  the adiabatic index. We use a Mach number  $\mathcal{M} = 3$  as observed in typical shocks (e.g. Markevitch & Vikhlinin 2007). The pressure profile before and after the jump is described by a power law with index 0 in the inner part (to avoid confusion with the signal that would arise from a steep core, as in the spherical gNFW profile), and index -2 in the outer part, respectively. The pressure is integrated along the line of sight and the resulting Compton parameter profile is used to generate the surface brightness. We consider a shock moving outward, with respect to the cluster center.

The toy model images are finally convolved with the NIKA beam and normalized to have a typical peak surface brightness of -1 mJy/beam. This corresponds to a Compton parameter of about  $10^{-4}$  and it is also the typical scale of the NIKA clusters.

#### 3.2. Application of the filters

We first consider the gNFW model (see the maps of Figure 2, top row). Because the pressure distribution is spherically symmetric, the surface brightness and the filtered maps are azimuthally symmetric (see the profiles of Figure ??, left pannel). The surface brightness profiles are peaked toward the center. We thus observe a ring with a radius that matches the filter plus beam size on the GGM map and profile. This means that at the angular scales recovered by NIKA and the redshift we consider, we are not able to observe a flattening in the profile in the core (if it exists), and the profile surface brightness appears always steeper as we get closer to the center. We observe a ring radius larger than the filter plus beam size, i.e. we detect a flattening in the

core, only when reaching redshifts lower than 0.5, in the case of the disturbed clusters pressure profile (i.e. the flatter that we consider here Arnaud et al. 2010). On larger scales, the GGM map smoothly vanishes. The null of the GGM map coincides with the cluster center due to smoothing. The typical scale of the gradient peak is 0.8–1.2 mJy/beam/arcmin, for a surface brightness normalized to -1 mJy/beam at the maximum decrement. The DoG maps allow us to extract the core signal, whose amplitude is typically 20–30% of that of the peak at our scales.

The middle row of Figure 2 provides the maps of the bimodal cluster. The GGM maps is elongated along the merger axis. The strong gradients on the north and south are due to the bar, that produces an artificial edge on the surface brightness (before filter and beam smoothing), and we also observe the gradient resulting of the gNFW cores on the east and west sides. The DoG map allows us to clearly define the different components that would not necessarily be obvious on the surface brightness map in particular in the presence of noise (see also Section 5).

The case of the main core plus extension is given on the bottom row of Figure 2. The GGM map presents two minima that correspond to the two cores and the gradient is reduced between the two sub-clusters, with respect to the single gNFW profile. Similarly to the bimodal case, the DoG map allow us to clearly identify the two components and their locations.

Figure 3 (right panel) presents the toy model and the corresponding filter response as a function of radius, in the case of the shock, similarly to the signal that one would extract along cones in the direction of the shock. It provides the pressure profile ( $P$ , as a function of the physical radius,  $r$ , in 3D), the surface brightness profile (as a function of the projected radius  $R$ , in 2D), and the filtered map profiles,  $\text{GGM}(R)$  and  $\text{DoG}(R)$ , respectively. The shock location is  $r_{\text{shock}} = 400$  kpc. Because of line of sight integration, the surface brightness profile does not present a trivial discontinuity. Instead, it progressively vanishes before the shock. The sharp discontinuities and peaks are then degraded due to instrumental beam smoothing. The GGM filter allow us to pick up the strong gradients in the map, and is thus well designed for highlighting shocks. It presents a peak associated to the shock, but it is not coincident with it (due to smoothing). The DoG filtered maps allows us to highlight compact sub-structures and the filter is efficient to pick up the cluster core. For such a shock and filter parameters, the GGM amplitude typically reaches 1-2 mJy/beam/arcmin, depending on the distance from the center via the amplitude of the surface brightness at the shock location. The DoG amplitude reaches -0.1-0.5 mJy/beam.

The different toy models show the expected signal after application of the filters under simplistic assumptions, but they correspond to typical features that one can expect in the NIKA sample. It is clear that the filtered maps provide a new way to look at our data, in particular in terms of morphological studies. At the angular scales probed by NIKA and the redshifts we consider (i.e., that of the NIKA sample), we can however see some limitations when pushing the extraction of the features to smaller angular scales. As a typical example, Figure 3 (right panel) shows that a shock will be hardly distinguishable from a ramp at redshift above 0.5. Similarly, the cluster core, even if purely spherical, will also show up at amplitudes similar to that of the signal arising from merging events that we want to extract.

The most accessible features correspond to scales of a few tens of arcsec, i.e. a few hundred kpc. After this preparatory exercise on toy models, we will next test the performances of the filters under controlled but realistic situations using cosmological hydrodynamic simulations.

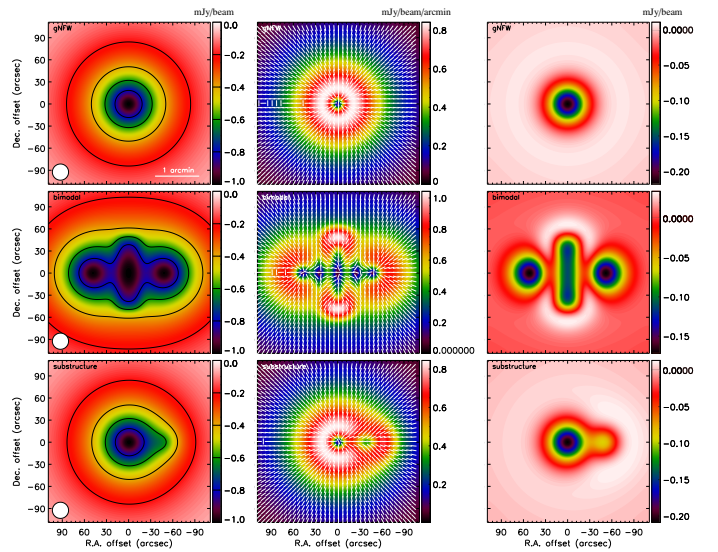


**Figure 2.** Surface brightness and GGM and DoG response to the tSZ signal expected for a spherically symmetric gNFW pressure profile (top), a bimodal cluster plus a pressure bar (middle), and a main core plus an extension (bottom). **Left:** tSZ simulated surface brightness. The white circle on the bottom left provides the beam FWHM. **Middle:** GGM filtered maps with  $\theta_0 = 15''$ . The white vectors represent the direction of the gradient,  $\Psi$ . **Right:** DoG filtered maps with  $\theta_1 = 15''$  and  $\theta_2 = 45''$ .

## 4. Application to hydrodynamical simulations

Before performing our analysis on the NIKA data, we test the behavior of the filters described in Section 2 by using realistic simulated cluster data. Such simulations also aid in the interpretation of the observed structures in real data, in addition to the toy models described in Section 3. To do so, we use synthetic tSZ images extracted from the RHAPSODY-G simulations for different cluster configurations.

### 4.1. Extraction of tSZ maps from the RHAPSODY-G simulations

The RHAPSODY-G simulations (Wu et al. 2013; Hahn et al. 2017) is a suite of cosmological hydrodynamics adaptive mesh refinement zoom simulations of ten massive clusters. The simulations include cooling and sub-resolution models for star formation and supermassive black hole feedback.

Boxes of co-moving volume (5 Mpc)<sup>3</sup> were used to extract Compton parameter maps around the clusters by integrating Eq 3 along a fixed line-of-sight direction, using the gas pressure in each grid cell. These maps were converted into surface brightness images, in the NIKA 150 GHz bandpasses (see the coefficient provided in Adam et al. 2017c). We neglect relativistic corrections, as they can only reduce the surface brightness by up to 8% for the hottest clusters at our frequency (Itoh & Nozawa 2003). The maps were produced for a large subset of the available simulation snapshots (about 150 per cluster), tracing the evolution of the clusters from redshift  $z \sim 1.5$  to  $z = 0$ . The knowledge of the cluster formation history from the simulation data is a key point for the interpretation of the maps.

### 4.2. Selection of a RHAPSODY-G sub-sample

A sub-sample of clusters was selected to assess the sub-structure detection in a quantitative way and to investigate the behavior

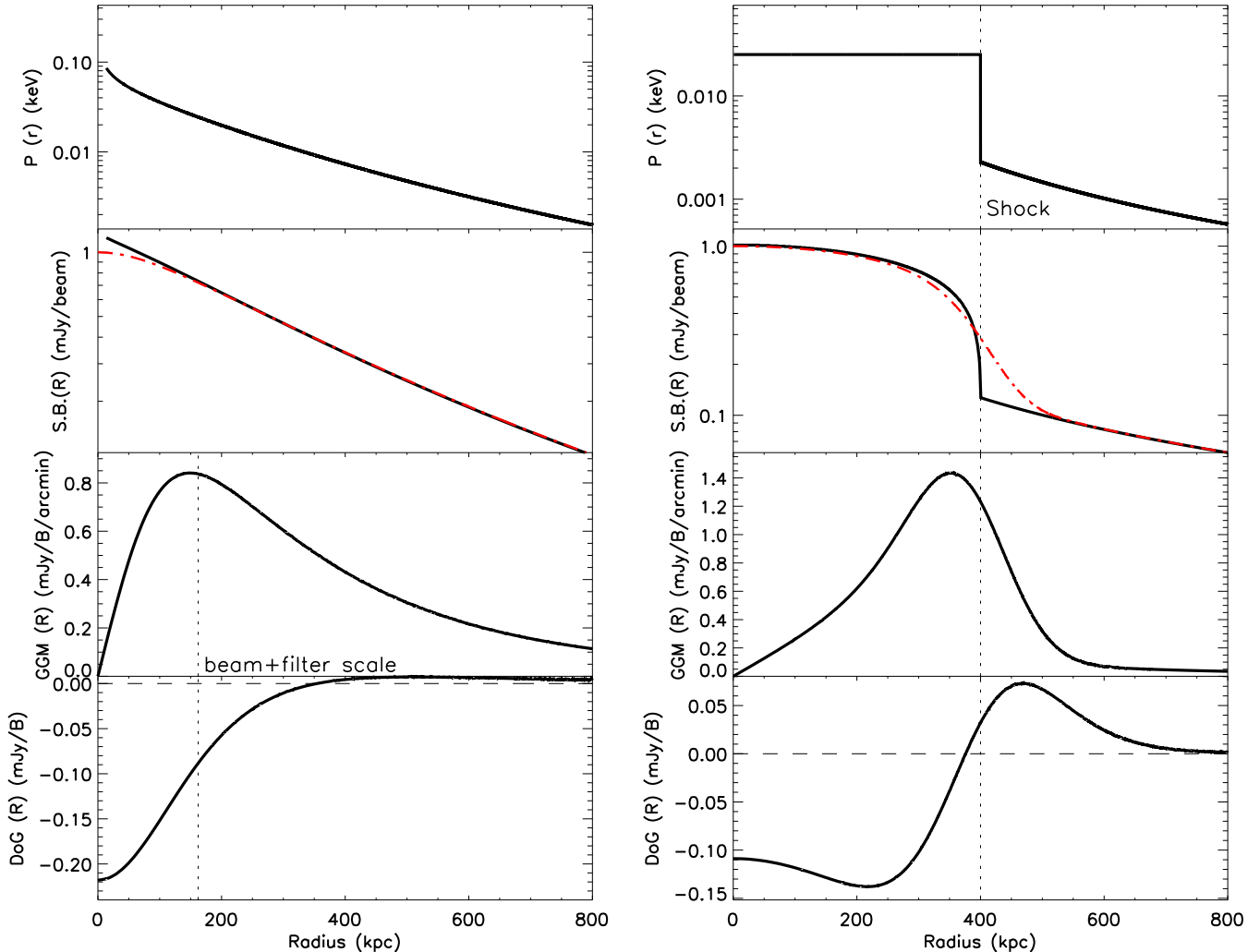


**Figure 3.** **Left:** GGM and DoG response to a gNFW radial pressure profile. The vertical dashed line provide the physical size corresponding to the 15 arcsec filter plus the NIKA beam size, at the cluster redshift. **Right:** GGM and DoG response to a shock propagating outward, in a radially symmetrical way, with Mach number  $M = 3$ . The shock position is given by the vertical dashed line. From top to bottom, we show the pressure, the surface brightness, the GGM and the DoG radial profile. In the surface brightness case, the thick black lines provide the raw profile while the thin red dashed-line accounts for beam smoothing. The pressure depends of the physical radius in 3D, while the other quantities depend on the projected radius, in 2D.

**Table 2.** Summary of the properties of the RHAPSODY-G selected cluster sample.

Name	$z$	kpc/arcsec	$M_{500}$ ( $10^{14} M_\odot$ )	$Y_{500}$ ( $10^{-3} \text{arcmin}^2$ )	Comments
RG361_00188	0.61	6.9	3.8	0.23	Very relaxed, elongated along the line-of-sight
RG474_00172	0.90	8.0	4.1	0.20	Major merger after the first crossing of the two main cores
RG377_00181	0.54	6.5	3.7	0.24	Multiple merger
RG448_00211	0.40	5.5	3.5	0.29	Pressure shell caused by the central AGN

of the filters in details (see Section 5 for the end-to-end processing of the simulations). The clusters were selected to match the redshift range of the NIKA sample (see Section 2.2) and to explore various cluster configurations. We thus restricted the RHAPSODY-G snapshots to the redshift range  $0.4 < z < 1$  and selected four distinct snapshots (see Figure 4), by visual inspection, for different clusters<sup>1</sup>:

<sup>1</sup> The 3-digit number after "RG" refers to the respective RHAPSODY-G halo, while the second 5-digit number refers to the snapshot number of the analyzed map.

1. **RG361\_00188:** a relaxed spherical cluster at redshift  $z = 0.61$ , with minimal merging activity since  $z \gtrsim 1$ . The cluster is slightly elongated along the line-of-sight.
2. **RG474\_00172:** a major merger at  $z = 0.90$ . The two main sub-clusters already passed through each other, the closest encounter happening at  $z \sim 0.95$ . The merger axis is close to the plane of the sky.
3. **RG377\_00181:** a triple-merger with two nearly equal mass objects and a smaller sub-group at  $z = 0.54$ . The two main sub-clusters have already experienced a first encounter at  $z \sim$

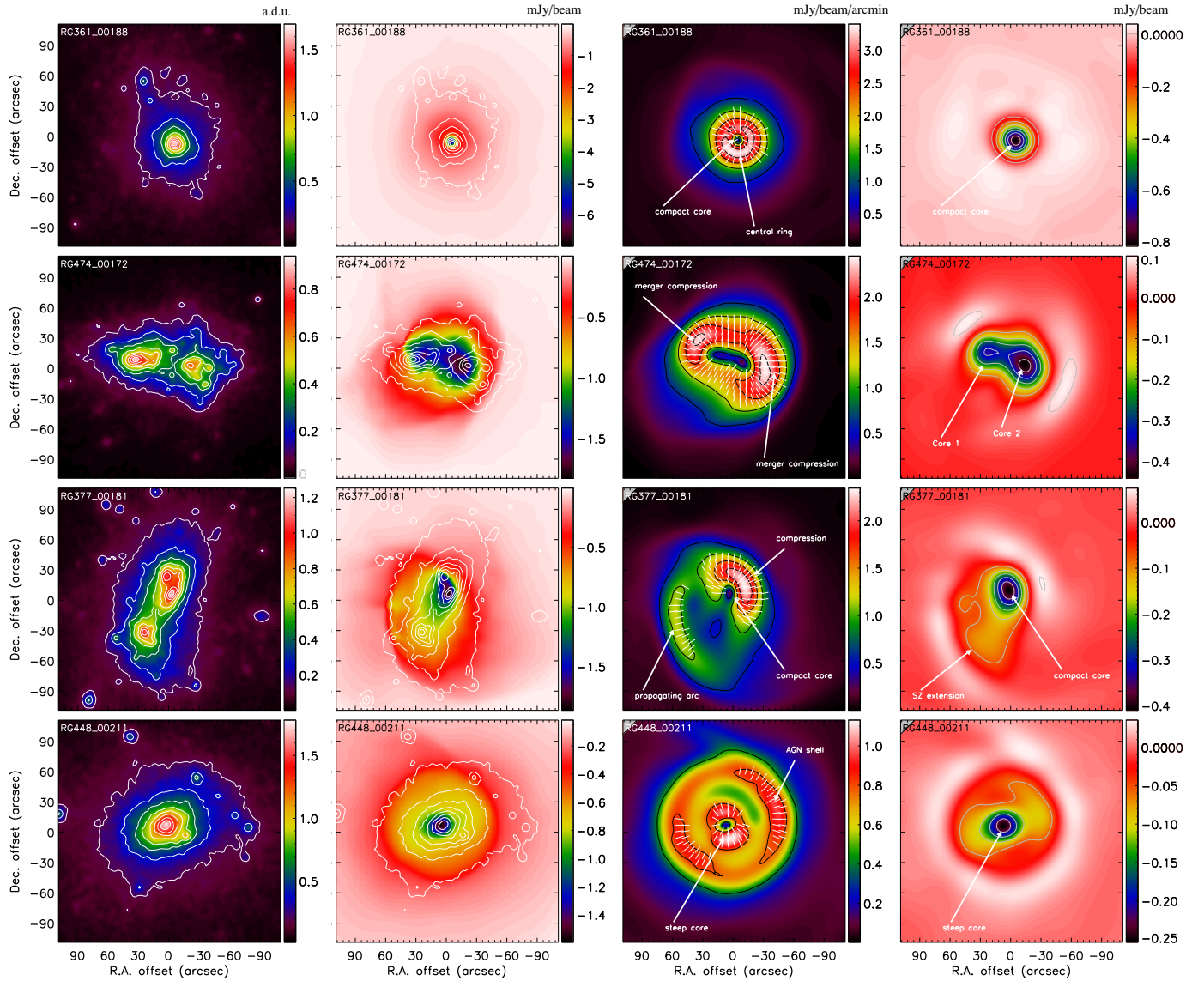


**Figure 4.** Application of the filtering algorithms to clusters from the RHAPSODY-G suite of simulations. From top to bottom, the clusters are RG361\_00188, RG474\_00172, RG377\_00181 and RG448\_00211 (see also Table 2 for the main properties of the sample). **Left:** projected dark matter density. Contours are linearly spaced. Units are arbitrary. **Middle left:** input raw tSZ surface brightness maps with dark matter map contours overlaid. Units are mJy/beam. **Middle right:** GGM filtered maps with  $\theta_0 = 15''$ . The white vectors represent the direction of the gradient,  $\Psi$ . Units are mJy/beam/arcmin. **Right:** DoG filtered maps with  $\theta_1 = 15''$  and  $\theta_2 = 45''$ . Units are mJy/beam. The contours provide the true signal-to-noise expected for the simulation of the observation of these sources done in Section 5. They are given by steps of  $2\sigma$  excluding 0 (see Section 5 for further discussions about the signal-to-noise estimates).

0.59, while the smaller group is spatially coincident (aligned) with one of the two main clusters.

4. **RG448\_00211:** a relaxed, slightly elliptical cluster, exhibiting strong AGN feedback at  $z = 0.40$ . This produces a pressure shell around the main core.

We note that the RHAPSODY-G cluster masses match well those of the NIKA sample at redshift zero, but they are lower by a factor of a few at the considered redshifts. Therefore the simulated surface brightnesses are also lower by a factor of  $\sim 2$ . The summary of the main properties of the four RHAPSODY-G selected clusters is provided in Table 2.

#### 4.3. Filter application to raw RHAPSODY-G tSZ images

We first apply the filters defined in Section 2 to the raw RHAPSODY-G surface brightness images (i.e. without includ-

ing noise or observational artifacts). The filtering parameters are set according to our baseline choice (Section 2.3.3), as optimized for the NIKA sample. Figure 4 provides images of the input surface brightness of the RHAPSODY-G selected sample, and the corresponding filtered maps together with the projected dark matter density distribution.

RG361\_00188 (relaxed) presents a very compact core and is azimuthally symmetric. The tSZ signal matches well that of the dark matter. As the steepness of the surface brightness profile increases toward the center, the corresponding GGM map is null at the cluster peak and exhibits a quasi perfect ring with radius matching the filter scale (see also the gNFW model of Figure 2), with a small excess in the south. The DoG map presents a single compact core component. The RG474\_00172 and RG377\_00181 (major and multiple mergers, respectively) tSZ maps show that the two clusters are both clearly non-spherical. The correspond-

ing dark matter maps reflect the presence of multiple sub-clusters and the dark matter distribution deviates significantly from that of the tSZ signal. The GGM maps provide additional information by highlighting regions of strong gas compression. In the case of the major merger, RG474\_00172, we observe a strongly elongated ring with two main pressure gradients in the east and west regions, comparable to the merger toy model of Figure 2 without the bar component. Discontinuities are observed in the simulation at these locations, but they are too close to the core to be distinguished from it considering our baseline scales, and the signal we observe results from the sum of the shocks and the gNFW-like steep cores, as an overall compression. In the case of the multiple merger, RG377\_00181, a strong gradient is visible in the west region, corresponding to the main core, and a  $\sim 70$  arcsec (460 kpc) long arc propagates through the ICM on the southeast sector, corresponding to another sub-cluster moving within the ICM of the main cluster and causing a shock. The DoG maps present a double peak structure, allowing us to quantitatively identify the two sub-clusters in the case of RG474\_00172. In contrast, one only finds a main core plus a weak extension in the case of RG377\_00181 (comparable to the main core plus extension toy model of Figure 2). RG448\_00211 appears to be relatively relaxed and azimuthally symmetric, in agreement with the dark matter distribution. However, the GGM map reveals, in addition to the steep core, the presence of a pressure shell responsible for a strong gradient ring extending 45 arcsec (250 kpc) away from the peak. This is due to the feedback from the central AGN onto the ICM, and possibly an artifact of the specific implementation of AGN feedback as a thermal blast-wave in these simulations. We also observe a plateau extending to 45 arcsec (250 kpc) radius on the DoG filtered map and we note that the core signal is slightly elongated with a main axis inclined by about 20 degrees with respect to the R.A. axis.

The morphologies seen in the filtered RHAPSODY-G sub-sample provide templates that we can compare to the structures observed in the real NIKA data. In practice, we performed this analysis using all available RHAPSODY-G snapshots and projected the data along three line-of-sight directions. Therefore, we dispose of a much larger variety of configurations, even if the four selected clusters already qualitatively sample most of the structures visible in the simulation, according to the selection of the sub-sample. These templates will allow us to better understand the physics at play in the NIKA clusters, in particular in merging systems. When using the tSZ signal as a tracer of the overall matter distribution (e.g. Adam et al. 2015, 2016; Ruppin et al. 2017), the application of such filters could also help to interpret scatters and biases between the total mass distribution and the tSZ signal, as such features reflect spatial misalignment between the dark matter distribution and the hot gas.

In summary, the GGM and the DoG filters allow strong gradient in the surface brightness (seen as ridges in the GGM maps), and tSZ peaks in the RHAPSODY-G images, respectively. They provide templates for interpreting features observed in the NIKA data in Section 6. These features correspond to shocks and gas compression regions induced by merging events, and the main cores of the merging sub-clusters, respectively. In the case of isolated spherical clusters, GGM features are also observed, showing up as rings around the tSZ peak.

## 5. Systematic effects and noise properties

In addition to the tSZ sub-structures, NIKA data are affected by several systematic effects that can potentially alter the reconstructed filtered images. In this Section we test the response of

the filters described in Section 2 to potential bouncing artifacts due to the transfer function of the NIKA processing, spatially correlated noise, and point source residuals.

### 5.1. NIKA processing of the RHAPSODY-G sub-sample

While the DoG filter is linear and preserves the gaussian nature of the noise, this is not the case for the GGM filter. Therefore, in order to validate the behavior of the filter, we use end-to-end realistic simulations of the observations and post-processing of the RHAPSODY-G sub-sample, including all the artifacts present in the real data, but for which the true input signal is known.

To obtain simulated observed surface brightness images, we make use of the real raw telescope time ordered data (TOD) collected for the cluster MACS J0717.5+3745 (the one with the largest observing time, see Section 6), in which we inject the signal corresponding to the considered RHAPSODY-G tSZ maps, according to the telescope scanning strategy. Prior to adding the simulated signal to the data, half of the TOD scans are multiplied by  $-1$  in order to cancel the astrophysical signal present in the real data, on the final co-added map. We aim at obtaining simulations corresponding to the highest signal-to-noise NIKA clusters. Therefore, before adding the simulated signal to the TOD, the noise is rescaled by the ratio of the RHAPSODY-G clusters peak surface brightness to the one of the deconvolved map of MACS J0717.5+3745 (typically a factor of  $\sim 2$ , see Section 4.2). The TOD are then processed similarly to the one of the real NIKA clusters (see Adam et al. 2015, for more details).

Finally, we obtain realistic maps of the RHAPSODY-G sub-sample, as if they were truly observed using NIKA, with a signal-to-noise peak of about 20, at 22 arcsec resolution. The maps, once deconvolved from the processing transfer function (see Section 5.2), are displayed in Figure 5, together with their GGM and DoG filtered maps obtained using our baseline parameter values (cf. Section 2.3.3). These maps can be compared to that of Figure 4 to validate our procedure, and they are used in the following sub-sections to quantify the properties of the filtered maps in the presence of systematic effects and noise.

### 5.2. Transfer function filtering

By construction, the zero level surface brightness of the NIKA maps is not defined. However, this does not affect the results presented in this paper since both the GGM and DoG filtering procedures are insensitive to zero level effects. In addition, the NIKA processing transfer function reduces the signal on scales that are larger than the instrument field of view ( $\sim 2$  arcmin). After deconvolution, small differences can remain between the deconvolved image and the original input image, due in particular to anisotropies in the scanning strategy and uncertainties in the estimated transfer function. However, these differences are mostly prominent on scales larger than the NIKA field of view, where filtering effects are important (Adam et al. 2015). By comparing the NIKA-like processed RHAPSODY-G sub-sample to the non-processed maps, we find that these differences have a negligible impact on the filter application with respect to the noise (see figures 4 and 5).

### 5.3. Noise spatial correlations and propagation through the filters

The NIKA noise is Gaussian and spatially correlated (Adam et al. 2016) but its behavior does not necessarily propagate in

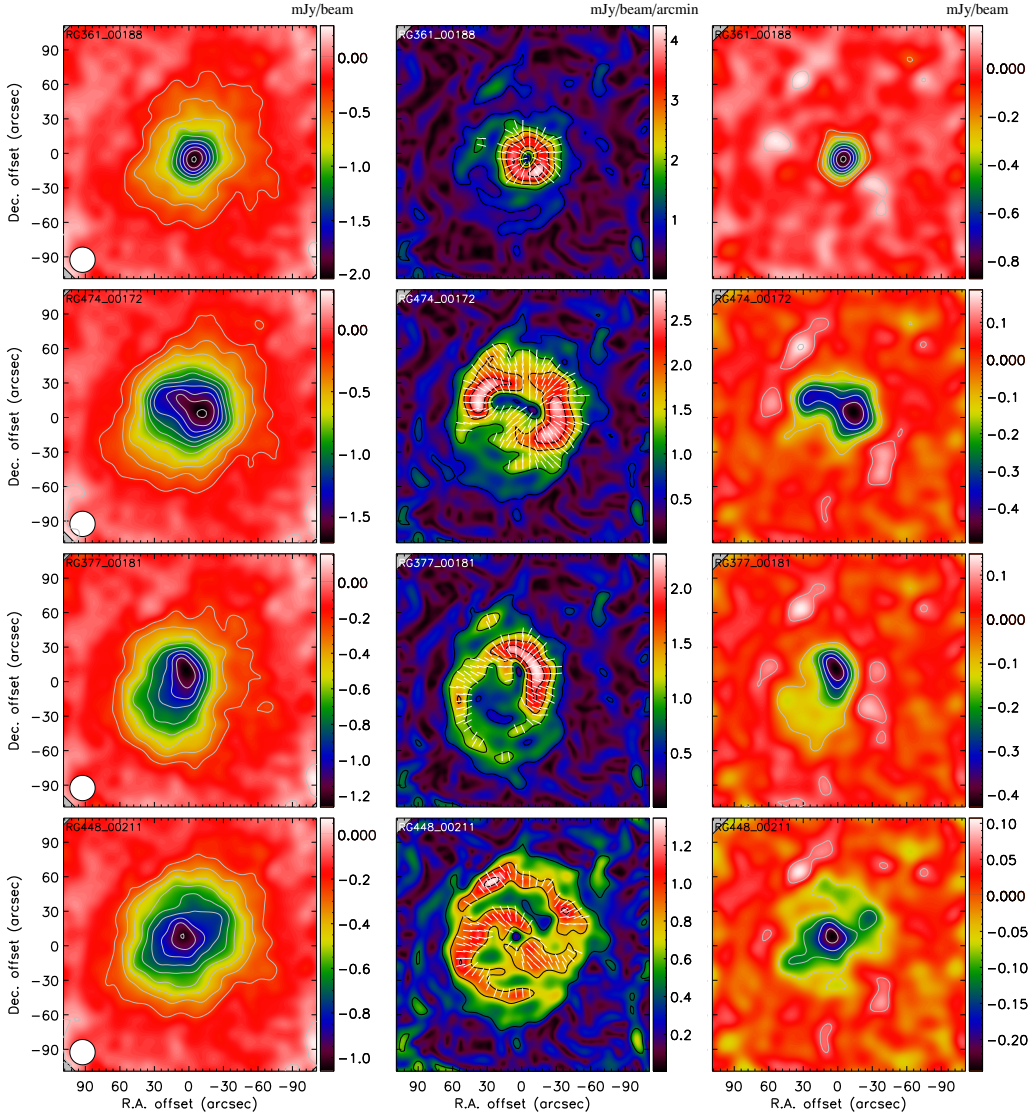


**Figure 5.** Same as figure 4 in the case of end-to-end processing of the simulated RHAPSODY-G sub-sample: surface brightness maps (left), GGM filtered maps (middle) and DoG filtered maps (right). From top to bottom, the clusters are RG361\_00188, RG474\_00172, RG377\_00181 and RG448\_00211 (see also Table 2 for the main properties of the sample). The surface brightness images are deconvolved from the transfer function (but not from the beam smoothing) and the signal-to-noise contours are estimated as in the case of real data (separated by steps of  $2\sigma$ ).

a trivial way under the application of the filters, especially in the case of the GGM filter, which is non-linear. In order to estimate the significance of the structures that we observe in Section 6, we use noise realizations of the surface brightness maps generated as described in Adam et al. (2016). They account for the map pixel-to-pixel correlated noise induced by residual atmospheric and electronic noise, the inhomogeneities of the noise due to the scanning strategy, and the contribution of the cosmic infrared background, which is non-negligible for the deepest observations. For each cluster, we produce a set of 1000 surface brightness noise realizations,  $N^{(i)}$ , which are deconvolved from the transfer function associated to the NIKA data processing similarly to their corresponding cluster data and used to estimate the noise in the filtered maps using the following procedure.

As the DoG filter is linear and preserves the noise Gaussianity, we process these surface-brightness-noise-only Monte Carlo realizations through the same filter as the data. Then, we estimate the respective DoG filtered maps standard deviation by taking the root-mean-square of all the processed Monte Carlo realizations, for each pixel of the map. The DoG

signal-to-noise ratio are straightforwardly obtained by normalizing the filtered cluster data by the standard deviation maps, and follow Gaussian statistics.

According to the definition of Eq 4, the noise of the GGM filtered maps depends on the surface brightness signal itself because of the non-linearity of the filter. Therefore, we use the observed signal as an estimate of the true signal,  $\hat{S}$ , to which we add the surface brightness noise realizations, prior to processing them through the GGM filter. The estimate of the filtered map noise contribution, from each Monte Carlo realization  $i$ , is then given by

$$N_{\text{GGM}}^{(i)} = (\hat{S} + N^{(i)})_{\text{GGM}} - \hat{S}_{\text{GGM}}, \quad (8)$$

where the index GGM corresponds to the filter application defined by Eq 4. For each pixel of the map, we compute  $\mu_{\text{GGM}}$  and  $\sigma_{\text{GGM}}$ , the mean and the standard deviation of the noise realizations  $N_{\text{GGM}}^{(i)}$  per map pixel, respectively. Accounting for the non-zero mean of the filtered map noise, the effective signal-to-noise

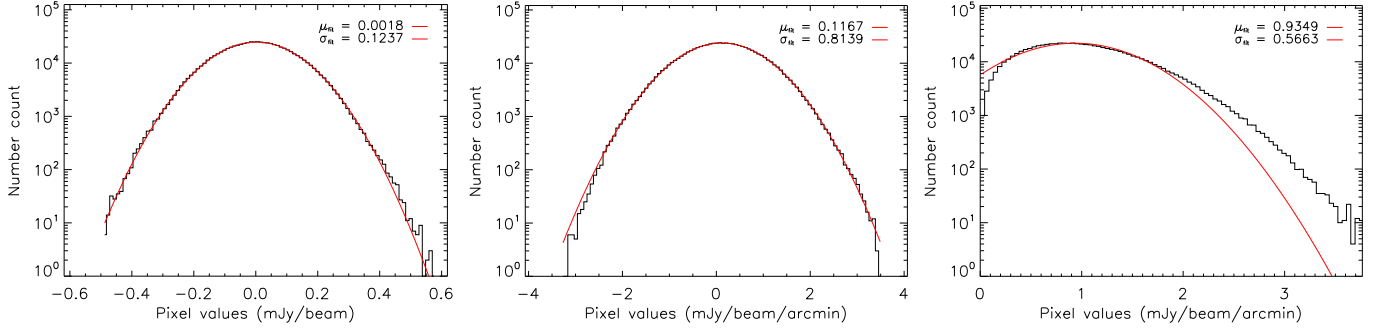


**Figure 6.** Noise distribution of all the pixels enclosed within 30 arcsec radius from the cluster center, in the case of CL J1226.9+3332, for our baseline filter parameters. The red curves provides the best Gaussian fit to the histograms. **Left:** DoG noise histogram. **Middle:** GGM noise histogram in the case of  $\hat{S}$  set to the observed signal of CL J1226.9+3332. **Right:** GGM noise histogram in the case where  $\hat{S} = 0$  in Eq 8.

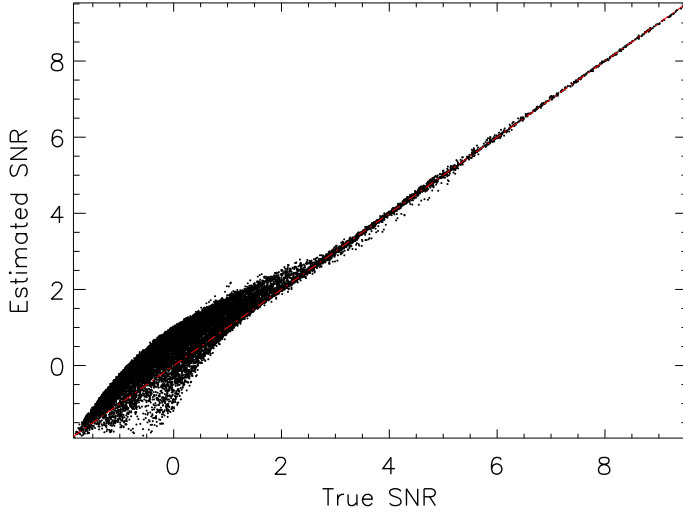


**Figure 7.** Comparison of the estimated GGM filtered maps signal-to-noise ratio as a function of the true signal-to-noise, using the RHAPSODY-G sub-sample. The estimated signal-to-noise is computed using the NIKA processed RHAPSODY-G sub-sample (Eq 9). The red dashed line represent the one to one correspondence. Each point corresponds to a pixel of the map.

ratio is defined as

$$\text{SNR}_{\text{GGM}} = \frac{\hat{S}_{\text{GGM}} - \mu_{\text{GGM}}}{\sigma_{\text{GGM}}}. \quad (9)$$

In practice, the estimated surface brightness signal is the sum of the true signal,  $S$ , and the noise,  $N$ , as  $\hat{S} = S + N$ . In the low surface brightness signal-to-noise regions,  $\hat{S}$  is therefore dominated by the noise, which can bias low the value of  $\mu_{\text{GGM}}$ . In the case of the RHAPSODY-G sub-sample, we also dispose of the true input surface brightness signal,  $\hat{S} = S$ , and we use it to compute the true signal-to-noise, to quantify the reliability of our signal-to-noise estimation procedure, as discussed below.

The noise distribution is illustrated in Figure 6 for both the GGM and the DoG filters. The data of CL J1226.9+3332 are used as an example, in the case of our baseline filter parameters (Section 2.3.3). The histograms account for the pixels that are enclosed within 30 arcsec from the cluster center, where the noise is homogeneous. In the case of the GGM filter, we consider both the possibility in which the cluster signal,  $\hat{S}$ , is set to the measured signal from CL J1226.9+3332, and where it is set

to zero in Eq 8, to illustrate the noise behavior in low signal-to-noise regions. As we can see, the DoG noise statistics (Figure 6, left panel) is described by a Gaussian distribution with a mean compatible with zero, by construction. The GGM noise distribution is well described by a Gaussian distribution in signal dominated regions (middle panel). However, as the signal vanishes, such as in the external regions, the noise becomes non Gaussian, its mean increases and the distribution gets positively skewed. Despite the fact that the non-zero mean of the noise is corrected for when computing the significance of the data, we note that the noise is boosted by up to 15% (in the wing of the distribution), in the extreme case of zero signal, with respect to what one would expect for Gaussian noise (Figure 6, red line).

The validation of the signal-to-noise reconstruction of the GGM filtered maps is illustrated in Figure 7. It shows the estimated signal-to-noise as a function of the true signal-to-noise, computed using the RHAPSODY-G sub-sample for which both  $\hat{S}$  and  $S$  are available. We can observe that in the low signal-to-noise regime, the estimated signal-to-noise is overall biased high, due to the fact that  $\mu_{\text{GGM}}$  is biased low. At higher signal-to-noise ( $\gtrsim 3$ ), the estimated signal-to-noise converges to the true signal-to-noise within a few percent. Our procedure is thus valid in this regime.

Finally, we use the end-to-end processed and filtered maps from a RHAPSODY-G sub-sample, shown in Figure 5, to check that the structures we recover are reliable. Indeed, above 3, the signal-to-noise of the recovered features is consistent with what we expect in the case of the raw maps of Figure 4 when using the true signal-to-noise.

#### 5.4. Point sources residuals

Foreground, background, or cluster-member galaxies can show up as point sources in tSZ images, which constitutes a well known potential bias. In the case of NIKA, these sources are subtracted either by fitting their flux together with the tSZ signal (Adam et al. 2015), or by modeling their Spectral Energy Distribution (SED) and fitting them to multi-wavelength photometric data to extrapolate their flux in the respective NIKA bands (see the method detailed in Adam et al. 2016). Even if such procedures provide a first good estimate of the contaminant, they are limited by the accuracy of the model to describe the data, the limited available extra data, and miscentering arising from limited accuracy in the source coordinate or telescope pointing precision. At 150 GHz, the contaminant sources are mostly radio galaxies, but infrared galaxies can also have a significant contribution.

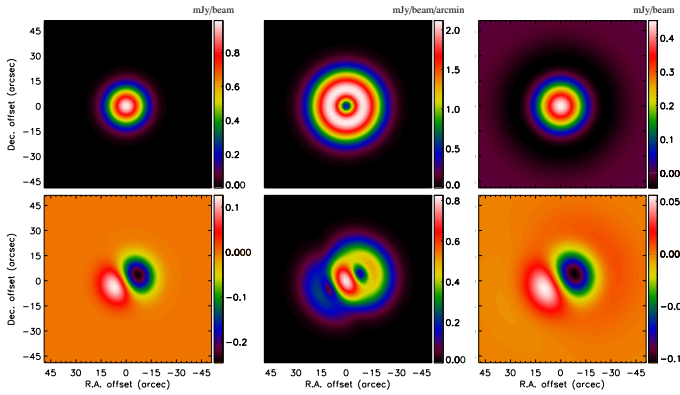


**Figure 8.** Application of the filters to point source residuals in case 1 (no source subtraction, top) and case 2 (source improperly subtracted, bottom). The input point source flux has been normalized to one. **Left:** input surface brightness map. **Middle:** GGM filtered map. **Right:** DoG filtered map.

We estimate the impact of residual point sources by considering the following approach in two upper limit cases:

1. Point sources below the detection threshold that are not subtracted: we simulate point sources with a flux of  $3\sigma$  times that of the noise rms, and assume that it is not subtracted from the tSZ map.
2. Point sources that are poorly subtracted: we assume a given degree of contamination by simulating a 3 mJy point source (the typical flux of the brightest radio sources observed in the NIKA clusters at 150 GHz), which we subtract assuming a flux that is off by 10%, and including a miscentering offset of 3 arcsec (the NIKA pointing accuracy for one scan [Catalano et al. 2014](#)).

As the GGM filter is not linear, the point source contamination induced by the application of the filter depends not only on the point sources themselves, but also on the local environment of the source. Therefore, we test both the case where the sources are simulated in the outskirts of the clusters, where the noise dominates, and within a few arcsec of the cluster core, where the signal dominates.

Using our baseline filter parameters, we find that the difference between the point-source-contaminated and the tSZ-only maps can reach deviations of up to  $4\sigma$ , both for the GGM and the DoG filters. As the signal-to-noise ratio of the simulated clusters is set to match the highest signal-to-noise NIKA clusters, it represents an upper limit of the contamination. In addition, the biases remain local on the maps and exhibit specific structures that are distinct from the ones that appear in the case of interacting clusters (ring-like shaped, azimuthally symmetric, or dipole-like at the scale of the filter, see figure 4). Nonetheless, point source residuals could mimic compact tSZ cores, at the scale of the beam. As we increase the filter scales, the signal arising from point source residuals quickly becomes insignificant. The signatures of point source residuals are illustrated in figure 8. Due to the GGM non linearity, the corresponding extra signal arising from point sources can slightly deviate from the one shown in figure 8.

We conclude that undetected or mismodeled point sources are an unavoidable potential bias. They can affect the interpretation of the signal at a level of a few  $\sigma$ , but they cannot lead to a mis-interpretation of the overall signal observed in tSZ maps as the contamination remains local. Other artifacts are expected to produce negligible signal in our filter data. Despite the non-

**Table 3.** Coordinates of the main X-ray peak.

Name	R.A.	Dec.	Reference
RX J1347.5-1145	13:47:30.575	-11:45:10.08	<i>Chandra</i> (ObsID3592)
MACS J1423.8+2404	14:23:47.908	+24:04:42.69	<i>Chandra</i> (ObsID4195)
MACS J0717.5+3745	07:17:31.740	+37:45:30.73	<i>Chandra</i> (ObsID4200)
PSZ1 G046.13+30.75	17:17:05.780	+24:04:26.00	<i>XMM-Newton</i> (ObsID0693661401)
PSZ1 G045.85+57.71	15:18:20.811	+29:27:39.10	<i>XMM-Newton</i> (ObsID0693661101)
CL J1226.9+3332	12:26:58.454	+33:32:48.36	<i>Chandra</i> (ObsID5014)

linearity of the GGM filter, we have developed a method to estimate the statistical significance of the corresponding signal that is accurate above signal to noise of three.

## 6. Application to the NIKA clusters sample

The NIKA surface brightness maps at 150 GHz are provided in Figure 9 together with the filter algorithms results. They are deconvolved from the processing transfer function, smoothed to an effective resolution of 22 arcsec FWHM and cleaned from point source contamination. The three clusters RX J1347.5-1145, MACS J1423.8+2404 and PSZ1 G046.13+30.75 have been imaged with NIKA. Despite the relatively low significance of this sub-sample (less than  $10\sigma$  per beam at the 22 arcsec resolution), we apply the GGM and DoG filter to the maps. We observe hints for internal structures, but only at low significance level, as briefly discussed below. The three other NIKA clusters, MACS J0717.5+3745, PSZ1 G045.85+57.71 and CL J1226.9+3332, present a peak significance larger than  $10\sigma$  at the 22 arcsec resolution, with a maximum of more than  $18\sigma$  for MACS J0717.5+3745 (see figure 9). This is comparable to the RHAPSODY-G processed tSZ maps of Figure 5 and we thus expect to be able to find sub-structure features at a similar significance within these clusters. The GGM and DoG filtered maps of the NIKA clusters are presented in Figure 9 for our baseline filter parameters. In the following sub-sections, we discuss the individual cluster analysis.

### 6.1. RX J1347.5-1145

RX J1347.5-1145 is a massive cluster at redshift 0.45, and one of the most luminous X-ray cluster. Being an extremely bright tSZ source, it has already been observed using the tSZ effect by several groups (e.g. [Pointecoutau et al. 1999](#); [Komatsu et al. 1999](#); [Mason et al. 2010](#); [Plagge et al. 2013](#); [Adam et al. 2014](#); [Sayers et al. 2016](#); [Kitayama et al. 2016](#)). RX J1347.5-1145 presents a dense core, but also shows an extension toward the southeast, which is associated with the merging of a sub-cluster. The tSZ peak is aligned with the southeast extension, corresponding to the overpressure caused by the merger in this region. This cluster was observed with an early setup of the NIKA instrument (band-pass, sensitivity, calibration procedure, see [Adam et al. 2014](#), for more details). In addition, the scanning strategy was not isotropic due to a mistake in the control software, leading to possible artifacts in the filtered map. Therefore, the application of the filtering algorithms on the NIKA map of RX J1347.5-1145 is meant to remain qualitative in this paper. The GGM filtered map presents a  $\gtrsim 2\sigma$  ridge ( $\gtrsim 4\sigma$  when using  $\theta_0 = 20$  arcsec), inclined by 40 degrees with respect to the Dec. axis, about 30 arcsec (178 kpc) east from the X-ray center. It could be associated to the eastern shock front seen in *Chandra* data by [Kreisch et al. \(2016\)](#), but deeper tSZ observation are necessary to confirm it. The DoG filtered map shows that the tSZ pressure in the

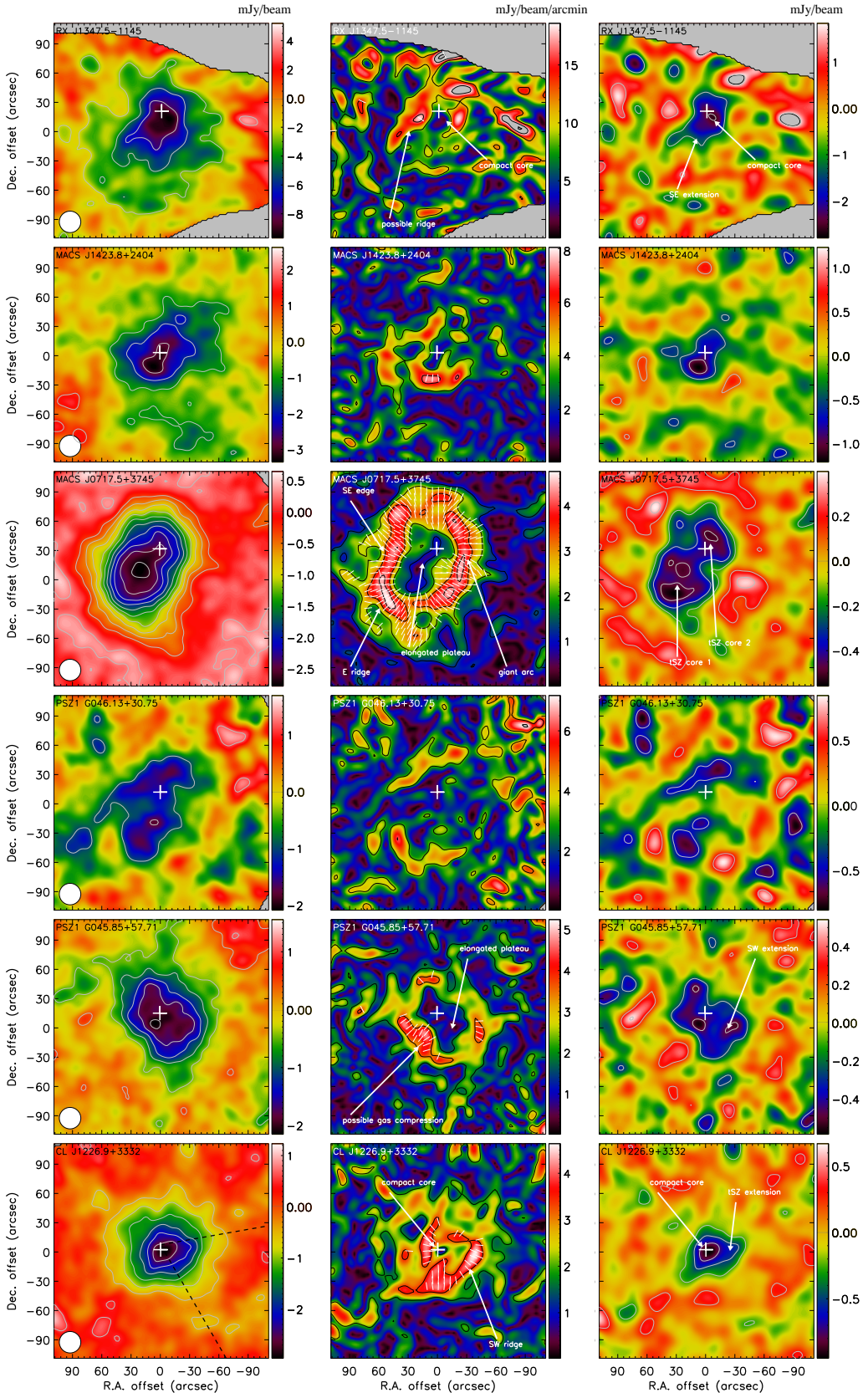


**Figure 9.** Redshift-ordered maps of the NIKA cluster sample at 150 GHz. **Left:** Surface brightness images. Each map has been smoothed to an effective angular resolution of 22 arcsec FWHM, as shown by the bottom left white circle. Point sources have been subtracted and the data have been deconvolved from the transfer function, but the zero level absolute brightness remains unconstrained. **Middle:** GGM filtered maps. **Right:** DoG filtered maps. In all cases, contours provide the signal-to-noise ratio, starting at  $\pm 2\sigma$  and increasing by  $2\sigma$  steps. The white crosses provide the main X-ray peak (see Table 3). In the case of MACS J0717.5+3745, the kSZ contribution is not accounted for in the map presented here (see Appendix B and Section 6.3 for more details). In the case of CL J1226.9+3332, the two dashed lines correspond to the cone used to define the GGM ridge region when extracting profiles in Figure 11.

cluster core is elongated from SE to NW. Large scales being filtered out, the morphology of the map compares well with that of MUSTANG (Mason et al. 2010) and ALMA (Kitayama et al. 2016) that are sensitive to smaller scales and intrinsically filter out large scales.

## 6.2. MACS J1423.8+2404

MACS J1423.8+2404 is a very relaxed system and a typical cool-core, at redshift 0.55. The corresponding NIKA observations and data reduction are detailed in Adam et al. (2016), including a detailed description of the cluster. The peak signal-to-noise ratio of the NIKA map reaches about 6 at the 22 arcsec resolution. The GGM and DoG maps do not allow us to identify sub-structures that deviate from that expected for a spherically symmetric object, within the noise fluctuations whose magnitude is large. Only a small GGM excess is visible in the south, but point source contamination (AGN and IR) is strong near the cluster center, and this could be due to mis-modeling of the contamination (see Adam et al. 2016, and the discussion of Section 5.4).

## 6.3. MACS J0717.5+3745

MACS J0717.5+3745 is one of the most disturbed clusters known to date. It is made of at least four interacting sub-clusters (Ma et al. 2009), and is thus an excellent target to search for compression regions, discontinuities and secondary peaks in tSZ maps. In addition to the systematic uncertainties discussed in Section 5, MACS J0717.5+3745 contains a significant amount of kinetic Sunyaev-Zel'dovich (kSZ, Sunyaev & Zeldovich 1980). Because of large uncertainties in the estimates of this contaminant, it is only possible to test the impact of the kSZ signal on our result by comparing the recovered signal in the cases with and without kSZ correction, as detailed in Appendix B. Since MACS J0717.5+3745 dispose of excellent X-ray data, we also provide a multi-wavelength view of the cluster together with our filtered maps in Figure 10.

The disturbed dynamical state of MACS J0717.5+3745 is obvious, as can be observed in Figure 9 and 10. The overall structure of the GGM and the DoG maps are the same for the case with and without kSZ, but the relative amplitude of the structures strongly depends on the correction (see Appendix B). Therefore, the kSZ contaminant only allows us a qualitative estimate of the gas inner structure. The GGM maps present two strong ridges on the east and southeast regions, of  $\sim 1$  arcmin (395 kpc) each ( $\text{SNR}_{\text{GGM}} > 8$ ). In addition, we observe a large arc ( $\sim 90$  arcsec) in the west sector that surrounds the X-ray main core. The southeast GGM ridge is spatially coincident with the southeast edge of the hot temperature bar caused by adiabatic compression (see Figure 10), and could trace a shock in this region. The eastern GGM ridge is nearly aligned with a radio relic (see, e.g. van Weeren et al. 2017), and both could be sourced by a shock caused by the ongoing merger. It also corresponds to a secondary vertical structure in the temperature map. The null of the gradient (i.e. flat surface brightness or constant projected ICM pressure) extends across all the brightest regions of the cluster in the case without kSZ correction, while it presents two nulls for the kSZ cleaned version of the map. In both cases, the main X-ray peak is aligned with a null region of the gradient, but we note that the X-ray structure is itself complex and presents several peaks. Both DoG maps highlight the presence of two main peaks in the pressure distribution (at  $> 4\sigma$ ). This was

also observed by Mroczkowski et al. (2012) using MUSTANG data. One of the peaks coincides with the main X-ray peak while the other one is coincident with the most massive sub-cluster, as identified from a strong lensing reconstruction (e.g. Limousin et al. 2016). It is also the location of the hottest region that shows adiabatically compressed gas from the merger of the two main clusters. Weaker extensions in the DoG map, such as the one extending to the southwest, coincide with secondary X-ray peaks and allow us to identify sub-structures also in the pressure distribution.

The GGM and DoG filtered maps of MACS J0717.5+3745 compare well to multiple major mergers as identified in the RHAPSODY-G simulation. They provide further insight into the gas structure of the cluster, with respect to the surface brightness image, by allowing us to identify regions of compressed gas. They are consistent with a major merger of two main sub-clusters and that of one (or more) additional sub-cluster likely to be smaller. Nevertheless, projection effects limit our interpretation of the data, in particular in the case of such a complex object. Using the filtered maps together with multi-wavelength data might in the future provide a better understanding of the ongoing merger scenario.

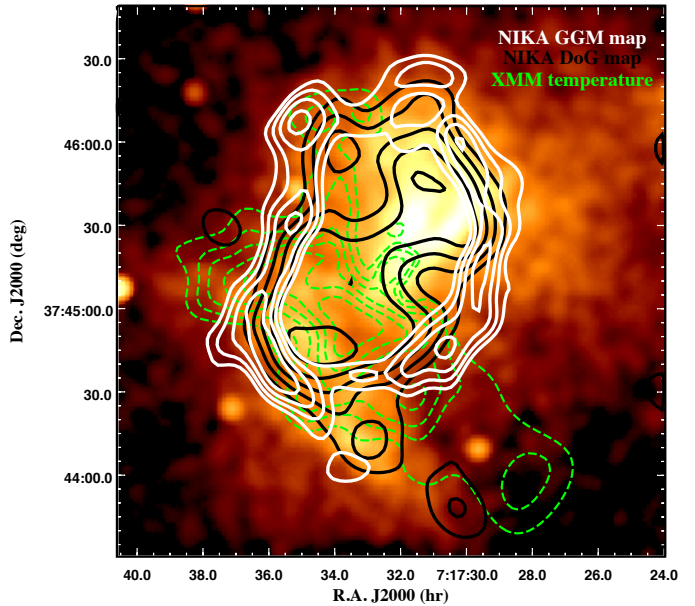


**Figure 10.** Multi-probe view of the cluster MACS J0717.5+3745: *Chandra* X-ray surface brightness image (ObsID4200), plotted on a square root scale (thus proportional to the projected density) with *XMM-Newton* temperature (red contours from Adam et al. 2017b) and the DoG (black contours) and GGM (white contours) maps overlaid.

## 6.4. PSZ1 G046.13+30.75

PSZ1 G046.13+30.75 is a *Planck*-discovered cluster (Planck Collaboration et al. 2014a), at redshift 0.55, and was observed during the same campaign as another NIKA cluster, PSZ1 G045.85+57.71 (see Ruppin et al. 2017, for more details). The observing weather conditions were unstable with a high opacity and the cluster significance barely reaches  $4\sigma$  per 22 arcsec FWHM beam at the peak on the NIKA map. The GGM and DoG filtered maps are consistent with noise.

### 6.5. PSZ1 G045.85+57.71

PSZ1 G045.85+57.71 is a *Planck*-discovered cluster ([Planck Collaboration et al. 2014a](#)), at redshift 0.61, and was observed during the same campaign as PSZ1 G046.13+30.75 (see [Ruppin et al. 2017](#), for more details). It was classified as a cool-core cluster based on its temperature and entropy profile, both fully consistent with the REXCESS cool-core sub-sample ([Böhringer et al. 2007; Arnaud et al. 2010; Pratt et al. 2010](#)). Its morphology is highly elliptical, with a main axis oriented about 45 degrees with respect to the R.A. axis, as can be observed in Figure 9, but [Ruppin et al. \(2017\)](#) do not find evidence for merging activity. The tSZ peak is consistent with that of the X-ray, and the tSZ elongation is mostly prominent toward the southwest.

The GGM map of PSZ1 G045.85+57.71 is that of an elongated ring following the morphology of the cluster. On the southeast region, we observe a stronger pressure gradient extending over about 45 arcsec (312 kpc) and reaching  $\text{SNR}_{\text{GGM}} = 5.8$ . In contrast to the RHAPSODY-G relaxed cluster RG361\_00188, the GGM map shows that the projected pressure is approximately constant (i.e., null of the gradient, or constant surface brightness), over a wide area from the X-ray core to the southwest extension. As PSZ1 G045.85+57.71 is a cool-core cluster, with a dense X-ray core, this indicates that the temperature rises in the southwest sector. The DoG map does not show the presence of any strong core and is consistent with the projected pressure being relatively constant from the X-ray core to the southwest extension. As a consequence of the lack of signal on small scales, the DoG map significance is relatively low, reaching only  $4\sigma$  at the peak. The main peak is located within a few arcsec of the X-ray core, but two secondary peaks are visible towards the southwest and on the north.

The GGM and DoG images of PSZ1 G045.85+57.71 are consistent with that of a merging sub-group falling from the southwest to the main cluster. It would be responsible for the local temperature rise and the gas overpressure on the southwest. Such scenarios are commonly observed in the RHAPSODY-G clusters. In contrast, relaxed RHAPSODY-G systems do not present similar features in their filtered maps, which reinforces the interpretation proposed above. Nevertheless, we note that the signal-to-noise ratio remains limited in the case of this cluster, and any stronger conclusions would require deeper data.

### 6.6. CL J1226.9+3332

CL J1226.9+3332 is a hot and massive high redshift cluster, at  $z = 0.89$ . It was discovered by ROSAT ([Ebeling et al. 2001](#)) and has been the object of several multi-wavelength studies since then. In particular, [Maughan et al. \(2007\)](#) identified a temperature excess in the southwest region from *XMM-Newton* and *Chandra* X-ray observations, in agreement with a tSZ sub-structure observed by MUSTANG ([Korngut et al. 2011](#)). This extension seen in the gas distribution is attributed to the merging of a smaller cluster that is visible from Hubble lensing data ([Jee & Tyson 2009](#)). NIKA was used to map the tSZ signal toward CL J1226.9+3332 as discussed in [Adam et al. \(2015\)](#), who also found an extension in the southwest region when subtracting a spherical model fitted to their data.

The large scale morphology of the NIKA map presented in Figure 9 shows that CL J1226.9+3332 is overall spherical and we observe a good match between the X-ray and tSZ peaks. This is confirmed by the GGM filtered map, where the location of the null of the gradient (the tSZ main peak), at the tSZ peak, is in excellent agreement with the X-ray peaks. The gradient is strong

around the core, indicating the presence of a compact pressure structure. However, we observe a strong GGM ridge in the southwest region ( $\text{SNR}_{\text{GGM}} = 5.7$ ), extending over about 45 arcsec (360 kpc). The DoG map agrees with CL J1226.9+3332 being dominated by a compact core ( $-7.7\sigma$ ) that matches the X-ray peak. It also shows an extension towards the west ( $> -4\sigma$ ).

In Figure 11, we provide the surface brightness and GGM profiles of CL J1226.9+3332 in the region of the GGM ridge and in the complementary region. The region is defined by the cone shown on the surface brightness image of Figure 9. It is designed to enclose the tSZ extension and to point in a direction perpendicular to the GGM ridge.

The signal observed in the GGM ridge region is in excellent agreement with that expected from a shock, as in Figure 3 (right panel). The GGM profile peaks at  $\theta = 37.5$  arcsec and we observe a discontinuity at the same radius in the surface brightness. On the contrary, the signal extracted from the complementary region is in good agreement with that of a relaxed spherical cluster. As expected in this case, the GGM signal peak is located at a radius that corresponds to the filter size (see also Figure 2 and Section 3) and the GGM profile smoothly vanishes as the radius increases. We note that presence of the GGM ridge could affect the pressure profile extraction as done in [Romero et al. \(2017\)](#). It could be responsible for the preferred large value of the  $\alpha$  gNFW parameter, which describes the width of the transition between the core and the outskirts.

The GGM and DoG analysis of CL J1226.9+3332 is fully consistent with that of a shock occurring within the merger scenario discussed above (see also [Adam et al. 2015](#), for more details). The structure observed in the signal matches well what is seen in the case of the RHAPSODY-G multiple merger RG377\_00181. Nonetheless, the strength of the tSZ extension with respect to the main cluster is larger in the case of CL J1226.9+3332 and the GGM ridge we observe is in a more compact configuration, closer to the core.

## 7. Discussions and perspectives

Cosmological studies using tSZ observations of clusters of galaxies generally rely on mass estimates based on various hypotheses, such as the hydrostatic equilibrium of the ICM or the 3D structure for lensing masses, and the self-similarity of the galaxy cluster population. These assumptions enable a calibration of the scaling law linking the integrated Compton parameter to the cluster total mass (see, e.g. [Arnaud et al. 2007; Arnaud et al. 2010; Planck Collaboration et al. 2013](#)), and using a universal pressure profile to compute the tSZ power spectrum (e.g. [Komatsu & Seljak 2002](#)). However, deviations from these hypotheses have already been identified and may lead to biases on cosmological parameters estimated using galaxy clusters (see, e.g. [Ichikawa et al. 2013; McDonald et al. 2014; Planck Collaboration et al. 2014b, 2016c,d](#)).

Deviations from hydrostatic equilibrium are expected for unrelaxed clusters where the non-thermal pressure content due to turbulence and bulk flows contributes significantly to the equilibrium of the gas in the gravitational potential (e.g. [Siegel et al. 2016](#)). Such effects suppress power principally on large scales in the tSZ power spectrum whereas AGN feedback has a significant impact on small scales (e.g. [Shaw et al. 2010](#)). Furthermore, the bias affecting the estimate of the cluster mass under the hydrostatic equilibrium assumption in unrelaxed clusters is expected to be higher than for relaxed clusters. The complex inner structure that can arise in the case of disturbed clusters can also affect

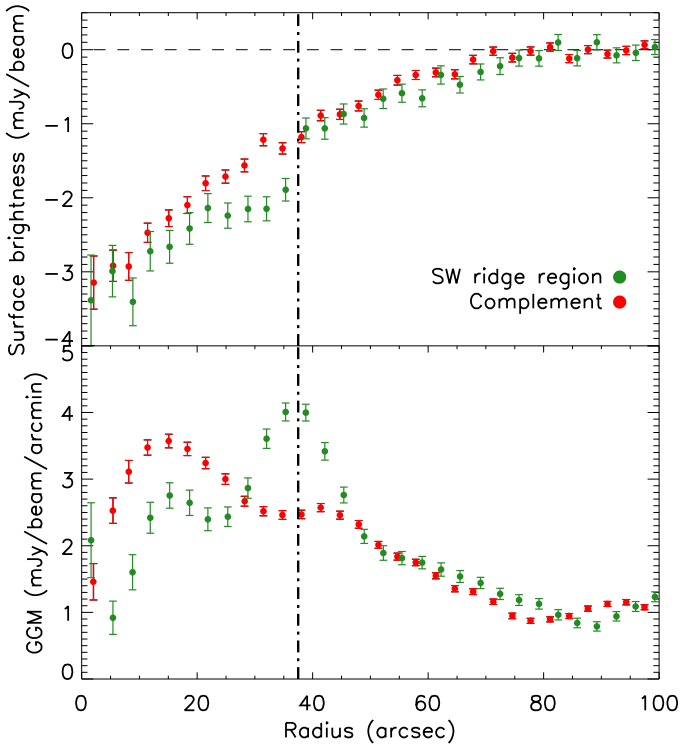


**Figure 11.** Comparison of the profile of CL J1226.9+3332 in the region of the GGM ridge (green) to its complement (red). The GGM ridge region is define in Figure 9, as the black dashed line on the surface brightness image. The dashed-dotted line correspond to the GGM ridge location. **Top:** surface brightness profile. **Bottom:** GGM profile.

lensing mass estimates. In this context, dynamical state indicators such as the features identified by the GGM and DoG filters are powerful tools to identify unrelaxed gas structures, which can help to understand the scatter and offset in the scaling relations.

While the tSZ surface brightness map of a cluster subject to AGN feedbacks can display an apparent relaxed morphology (see the cluster RG448\_00211 in Figure 4), the GGM map of this system reveals a characteristic ring feature which is not observed for a fully relaxed cluster (see the cluster RG361\_00188 in the same figure). The GGM map can then be used as a dynamical indicator to identify unrelaxed ICM regions in cluster outskirts and could therefore be linked to the amplitude of the hydrostatic bias.

Information on the dynamical state of the ICM is also given by the comparison of the distinct projected distributions of gas and dark matter. In the case of relaxed systems such as RG361\_00188, the gas distribution follows the one of the dark matter density, contrarily to major mergers or clusters with disturbed outskirts. Although the tSZ surface brightness map does not enable to constrain the dark matter density distribution, the gas compression direction provided by both the GGM and DoG maps can give information on the projected shape of the underlying gravitational potential. For example, while the apparent ICM morphology of the cluster RG448\_00211, in Figure 4, is azimuthally symmetric, the DoG map of this cluster displays an elliptical morphology with a major axis direction matching the one of the dark matter density distribution. The features in the DoG filter maps can therefore be used as a morphology indicator to identify potential deviations between the gas and the dark matter distribution.

Constraining the distribution of the cluster merger rate in large ranges of halo mass and redshift is of key importance to improve our understanding of the formation of large-scale structures (e.g. Cassano et al. 2016). The GGM map of the head-on merger RG474\_00172 (see Figure 5) displays a characteristic bimodal distribution giving the locations of high gas compression. Such information is not provided by the tSZ surface brightness map obtained after the end-to-end processing of the RHAPSODY-G simulated cluster. The GGM filter could therefore be used to improve on the identification of mergers by discriminating relaxed elongated ICM and major mergers.

The gas compression intensity, given by the amplitude of the gradient in the GGM maps, could also be compared to radio relic observations (e.g. van Weeren et al. 2010). The identification of a correlation between the two observables would enable to link the amplitude of the gradient in the GGM maps to the Mach number and therefore to the projected gas velocity. Such information would greatly enhance the understanding of structure assembly especially when combined with the gas line of sight velocity provided by kSZ effect observations.

## 8. Summary and conclusions

The tSZ effect provides a direct observable for the ICM pressure in galaxy clusters. In order to search for pressure sub-structures, which are related to the formation history of the clusters, we have applied filtering methods to resolved NIKA tSZ maps of six galaxy clusters at intermediate and high redshift. The same methods were applied to toy models and to the RHAPSODY-G hydrodynamical simulations in order to better interpret our results. Additionally, a careful investigation of the impact of possible systematic effects was performed. We considered contamination from compact sources, the filtering due to the NIKA processing, and the propagation of the spatially correlated noise.

While half of the clusters in the NIKA sample do not present sufficiently high signal-to-noise ratio to enable the identification of internal pressure structures with confidence, the three others show significant features that are not visible in the raw tSZ maps. The observed structures show signatures that are similar to the ones observed in the RHAPSODY-G simulations where they can be clearly attributed to compressions and shocks in the hot gas due to merging events. The potential point source residual contamination is unlikely to cause such structures because its signature is different from the one we observe, and expected to be subdominant. Similarly, we find that the effects of the NIKA processing are not significant at the scales of the observed structures and are subdominant given the available signal-to-noise ratio. Finally, we account for spatial correlations of the noise in order to assess the significance of the detections.

The three highest signal-to-noise clusters in our sample, MACS J0717.5+3745 at  $z = 0.54$ , PSZ1 G045.85+57.71 at  $z = 0.61$  and CL J1226.9+3332 at  $z = 0.89$ , were investigated in more depth. MACS J0717.5+3745 is clearly disturbed at all scales probed by NIKA. Three strong pressure gradient features are observed in the northwest, east, and southeast sectors, using the GGM filter. We also identified two main peaks in the pressure distribution from the DoG filtered map, which are associated with sub-groups seen at other wavelengths. PSZ1 G045.85+57.71 is elongated on large scales, but we do not observe significant sub-clumps. A GGM ridge is observed in the southeast of the cluster, potentially indicating ongoing merging activity. CL J1226.9+3332 appears to be relaxed on large scales, but the GGM filtered map shows a  $\sim 45$  arcsec (360 kpc) long GGM ridge in the west region associated with an elongation of

the gas on small scales as observed in the DoG filtered map. Its signature is in excellent agreement with that of a shock.

The combined high angular resolution and high sensitivity of current tSZ data has now reached a state where the detailed study of the ICM structure of galaxy clusters is possible up to intermediate and high redshifts. In the case of our sample, significant sub-structures start to be visible for clusters with a peak signal-to-noise of  $\gtrsim 10$ , per  $\sim 22$  arcsec beam.

Our analysis shows that it is possible to explore the details of cluster assembly in distant clusters using deep tSZ imaging. New generation instruments, such as NIKA2 (Calvo et al. 2016; Catalano et al. 2016; Adam et al. 2017a) at the IRAM 30m telescope, are expected to provide unprecedented high sensitivity tSZ data at high angular resolution. NIKA2 observations (such as the ones of the tSZ large program, Comis et al. 2016; Mayet et al. 2017) should therefore allow for in-depth investigations of the inner structure of the ICM pressure of a cosmologically representative cluster sample. Currently, the sample that we used in this paper is limited to redshifts larger than 0.45, at which the 18 arcsec FWHM NIKA resolution at 150 GHz corresponds to about 100 kpc. With an instantaneous field of view of 6.5 arcmin, NIKA2 will also allow us to observe lower redshift clusters more easily, and thus enable the access to smaller physical scales at similar integration time. At intermediate and high redshift, the mapping speed should increase by a factor of up to  $\sim 10$  from NIKA to NIKA2, thus providing very high signal-to-noise images in very short time.

**Acknowledgements.** We would like to thank the IRAM staff for their support during the campaigns. The NIKA dilution cryostat has been designed and built at the Institut Néel. In particular, we acknowledge the crucial contribution of the Cryogenics Group, and in particular Gregory Garde, Henri Rodenas, Jean Paul Leggeri, Philippe Camus. This work has been partially funded by the Foundation Nanoscience Grenoble, the LabEx FOCUS ANR-11-LABX-0013 and the ANR under the contracts "MKIDS", "NIKA" and ANR-15-CE31-0017. This work has benefited from the support of the European Research Council Advanced Grants ORISTARS and M2C under the European Union's Seventh Framework Programme (Grant Agreement nos. 291294 and 340519). We acknowledge fundings from the ENIGMASS French LabEx (B. C. and F. R.), the CNES post-doctoral fellowship program (R. A.), the CNES doctoral fellowship program (A. R.) and the FOCUS French LabEx doctoral fellowship program (A. R.). E. P. acknowledges the support of the French Agence Nationale de la Recherche under grant ANR-11-BS56-015. OH acknowledges funding from the European Research Council (ERC) under the European Union's Horizon 2020 research and innovation programme (grant agreement No 679145, project COSMO\_SIMS). D.M. acknowledges support from the Swiss National Science Foundation (SNSF) through the SNSF Early Postdoc and Advanced Postdoc Mobility Fellowships.

## References

- Adam, R. et al. 2017a, ArXiv e-prints, 1707.00908  
 —. 2017b, ArXiv e-prints, 1706.10230  
 —. 2017c, A&A, 598, A115, 1606.07721  
 —. 2016, A&A, 586, A122, 1510.06674  
 —. 2015, A&A, 576, A12, 1410.2808  
 —. 2014, A&A, 569, A66, 1310.6237  
 Allen, S. W., Evrard, A. E., & Mantz, A. B. 2011, ARA&A, 49, 409, 1103.4829  
 Arnaud, M., Pointecouteau, E., & Pratt, G. W. 2007, Astron. Astrophys., 474, L37, 0709.1561  
 Arnaud, M., Pratt, G. W., Piffaretti, R., Böhringer, H., Croston, J. H., & Pointecouteau, E. 2010, A&A, 517, A92, 0910.1234  
 Basu, K., Sommer, M., Erler, J., Eckert, D., Vazza, F., Magnelli, B., Bertoldi, F., & Tozzi, P. 2016, ApJ, 829, L23, 1608.05413  
 Birkinshaw, M. 1999, Phys. Rep., 310, 97, arXiv:astro-ph/9808050  
 Böhringer, H. et al. 2007, A&A, 469, 363, astro-ph/0703553  
 Bourdin, H., Mazzotta, P., & Rasia, E. 2015, ApJ, 815, 92, 1601.06323  
 Calvo, M. et al. 2016, Journal of Low Temperature Physics, 184, 816, 1601.02774  
 Cassano, R., Brunetti, G., Giocoli, C., & Ettori, S. 2016, Astron. Astrophys., 593, A81, 1606.07293  
 Catalano, A. et al. 2016, ArXiv e-prints, 1605.08628  
 —. 2014, A&A, 569, A9, 1402.0260  
 Comis, B. et al. 2016, ArXiv e-prints, 1605.09549  
 Dicker, S. R. et al. 2014, in Proc. SPIE, Vol. 9153, Millimeter, Submillimeter, and Far-Infrared Detectors and Instrumentation for Astronomy VII, 91530J  
 Ebeling, H., Jones, L. R., Fairley, B. W., Perlman, E., Scharf, C., & Horner, D. 2001, ApJ, 548, L23, astro-ph/0012175  
 Fabian, A. C. 2012, ARA&A, 50, 455, 1204.4114  
 Hahn, O., Martizzi, D., Wu, H.-Y., Evrard, A. E., Teyssier, R., & Wechsler, R. H. 2017, MNRAS  
 Ichikawa, K., et al. 2013, Astrophys. J., 766, 90, 1302.0095  
 Itoh, N., & Nozawa, S. 2003, ArXiv Astrophysics e-prints, astro-ph/0307519  
 Jee, M. J., & Tyson, J. A. 2009, ApJ, 691, 1337, 0810.0709  
 Kitayama, T. et al. 2016, PASJ, 68, 88, 1607.08833  
 Komatsu, E., Kitayama, T., Suto, Y., Hattori, M., Kawabe, R., Matsuo, H., Schindler, S., & Yoshikawa, K. 1999, ApJ, 516, L1, astro-ph/9902351  
 Komatsu, E., & Seljak, U. 2002, Mon. Not. Roy. Astron. Soc., 336, 1256, astro-ph/0205468  
 Korngut, P. M. et al. 2011, ApJ, 734, 10, 1010.5494  
 Kravtsov, A. V., & Borgani, S. 2012, ARA&A, 50, 353, 1205.5556  
 Kreisch, C. D., Machacek, M. E., Jones, C., & Randall, S. W. 2016, ApJ, 830, 39, 1607.04674  
 Limousin, M. et al. 2016, A&A, 588, A99, 1510.08077  
 Ma, C.-J., Ebeling, H., & Barrett, E. 2009, ApJ, 693, L56, 0901.4783  
 Markevitch, M., & Vikhlinin, A. 2007, Phys. Rep., 443, 1, astro-ph/0701821  
 Mason, B. S. et al. 2010, ApJ, 716, 739  
 Maughan, B. J., Jones, C., Jones, L. R., & Van Speybroeck, L. 2007, ApJ, 659, 1125, astro-ph/0609690  
 Mayet, F. et al. 2017, ArXiv e-prints, 1709.01255  
 McDonald, M., et al. 2014, Astrophys. J., 794, 67, 1404.6250  
 Monfardini, A. et al. 2011, ApJS, 194, 24, 1102.0870  
 Mroczkowski, T. et al. 2012, ApJ, 761, 47, 1205.0052  
 Nagai, D., Vikhlinin, A., & Kravtsov, A. V. 2007, ApJ, 655, 98, astro-ph/0609247  
 Plagge, T. J. et al. 2013, ApJ, 770, 112, 1203.2175  
 Planck Collaboration et al. 2014a, A&A, 571, A29, 1303.5089  
 —. 2014b, A&A, 571, A20, 1303.5080  
 —. 2013, A&A, 550, A131, 1207.4061  
 —. 2016a, A&A, 594, A27, 1502.01598  
 —. 2016b, A&A, 594, A13, 1502.01589  
 —. 2016c, A&A, 594, A24, 1502.01597  
 —. 2016d, A&A, 594, A22, 1502.01596  
 Pointecouteau, E., Giard, M., Benoit, A., Désert, F. X., Aghanim, N., Coron, N., Lamarre, J. M., & Delabrouille, J. 1999, ApJ, 519, L115  
 Pratt, G. W. et al. 2010, A&A, 511, A85, 0909.3776  
 Romero, C. et al. 2017, ArXiv e-prints, 1707.06113  
 Ruppini, F. et al. 2017, A&A, 597, A110, 1607.07679  
 Sanders, J. S., Fabian, A. C., Russell, H. R., Walker, S. A., & Blundell, K. M. 2016, MNRAS, 460, 1898, 1605.02911  
 Sarazin, C. L. 2002, in Astrophysics and Space Science Library, Vol. 272, Merging Processes in Galaxy Clusters, ed. L. Feretti, I. M. Gioia, & G. Giovannini, 1–38, astro-ph/0105418  
 Sayers, J. et al. 2013, ApJ, 778, 52, 1312.3680  
 —. 2016, ApJ, 820, 101, 1509.02950  
 Shaw, L. D., Nagai, D., Bhattacharya, S., & Lau, E. T. 2010, Astrophys. J., 725, 1452, 1006.1945  
 Siegel, S. R., et al. 2016, 1612.05377  
 Sunyaev, R. A., & Zeldovich, I. B. 1980, MNRAS, 190, 413  
 Sunyaev, R. A., & Zel'dovich, Y. B. 1972, Astrophys. Space Phys. Res., 4, 173  
 van Weeren, R. J. et al. 2017, ApJ, 835, 197, 1701.04096  
 van Weeren, R. J., Rotgering, H. J. A., Bruggen, M., & Hoeft, M. 2010, Science, 330, 347, 1010.4306  
 Wu, H.-Y., Hahn, O., Wechsler, R. H., Mao, Y.-Y., & Behroozi, P. S. 2013, ApJ, 763, 70, 1209.3309

## Appendix A: Impact of the filter parameters

In Figure A.1, we provide the extracted filtered signal as a function of the filtering parameters in the case of CL J1226.9+3332. As the size of the filters increases, the detection strength increases, but the small scale signal we aim at extracting get washed out. The baseline parameters chosen in this paper correspond to the second row.

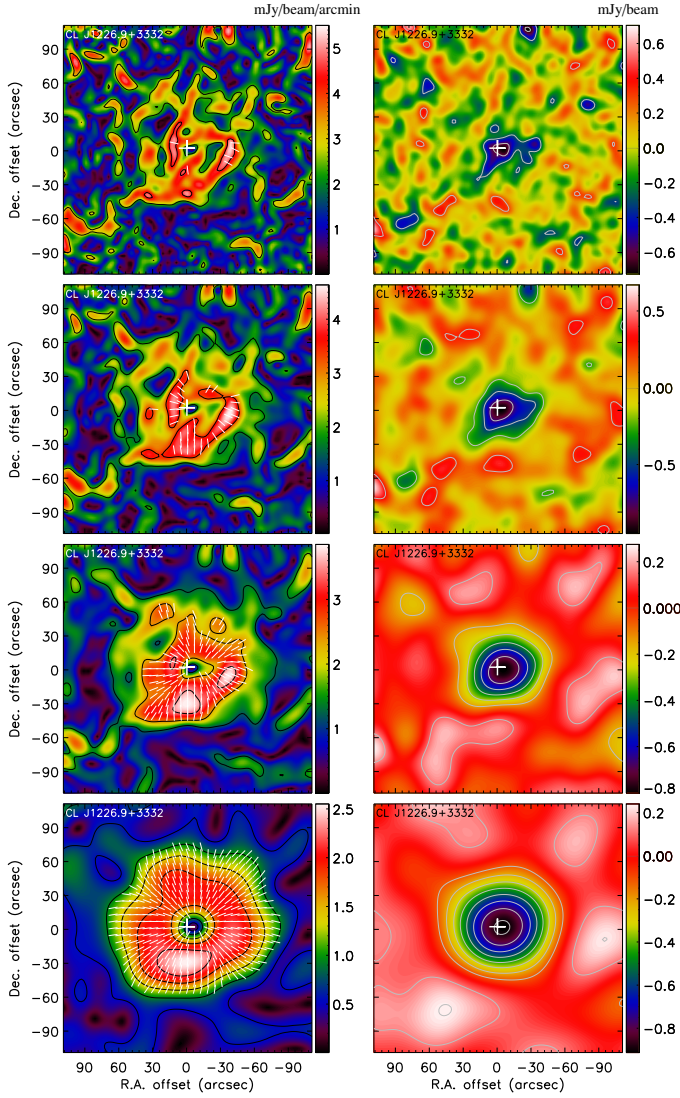


**Figure A.1.** Evolution of the GGM (left) and DoG (right) filtered maps of CL J1226.9+3332 as a function of the filter parameters. From left to right, the parameters are  $(\theta_0, \theta_1, \theta_2) = (12, 10, 30)$  arcsec,  $(\theta_0, \theta_1, \theta_2) = (15, 15, 45)$  arcsec,  $(\theta_0, \theta_1, \theta_2) = (20, 30, 60)$  arcsec and  $(\theta_0, \theta_1, \theta_2) = (40, 50, 100)$  arcsec.

## Appendix B: Impact of kSZ signal in MACS J0717.5+3745

The surface brightness of MACS J0717.5+3745 is affected by kSZ signal, and it is the only cluster for which an individual kSZ detection has been obtained to date (Mroczkowski et al. 2012; Sayers et al. 2013; Adam et al. 2017c). The kSZ signal is related to the gas density and line-of-sight velocity and has to be considered in order to study the pressure structure via the tSZ signal. Mroczkowski et al. (2012), Sayers et al. (2013) and Adam et al. (2017c) have obtained several kSZ signal models, but they are all limited by the large uncertainties in their best-fit parameters and are subject to strong assumptions in the gas modeling. Therefore, it is only possible to test the impact of the kSZ signal on our result by comparing the recovered sub-structures in the cases with and without kSZ correction. We thus produce a kSZ clean map of MACS J0717.5+3745 using the best-fit kSZ model from Adam et al. (2017c) to do so. Figure B.1 provides the surface brightness and filtered maps of MACS J0717.5+3745 in the case where the kSZ signal model has been subtracted to the data. The overall

structure is similar to that observed in Figure 9, where no correction is applied, but the magnitude of the different structures is significantly affected. See Section 6.3 for discussions.

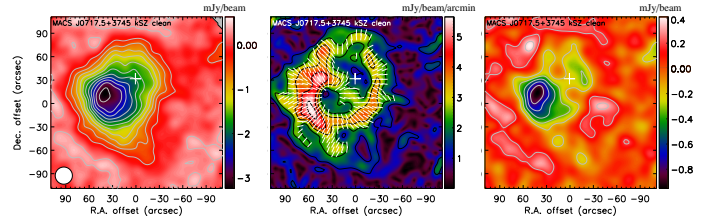


**Figure B.1.** Surface brightness (left), GGM (middle) and DoG (right) maps of MACS J0717.5+3745 in the case of kSZ correction applied. See figure 9 for further details.